Regenerative Therapy 30 (2025) 558–574

Contents lists available at ScienceDirect

Regenerative Therapy

journal homepage: www.elsevier.com/locate/reth

From an Antimicrobial Agent to a constituent of 3D Printed Heterogenous Scaffolds Stimulating Bone Characteristics: An In-vitro and Animal model evaluation

Shahad Ahmed Daood [a], Martha Then Xin Yi [a], Nicole Wen Ce Mun [a], Sharjeel Ilyas [b], Lee Yin Shien [a], Oh Jia En [a], Syed Saad Bin Qasim [c], Yichen Dai [d], Galvinderjeet Kaur Grewal [a], Ng Mei Liit [a], Gopu Sriram [d,e], Malikarjuna Rao Pichika [f], Kit-Kay Mak [f], Ranjeet Ajit Bapat [a], Zeeshan Sheikh [g,h,i,j,*], Umer Daood [a,k,**]

[a] Restorative Dentistry Division, School of Dentistry, International Medical University Kuala Lumpur, 126, Jalan Jalil Perkasa 19, Bukit Jalil, 57000, Wilayah Persekutuan Kuala Lumpur, Malaysia
[b] Oral Biology, Akhtar Saeed Medical and Dental College, Lahore, Pakistan
[c] Department of Bioclinical Sciences, College of Dentistry, Kuwait University, Kuwait City, Kuwait
[d] Discipline of Oral Sciences, Faculty of Dentistry, National University of Singapore, Singapore
[e] NUS Centre for Additive Manufacturing (AM.NUS), National University of Singapore, Singapore
[f] School of Pharmacy, IMU University KualaLumpur, KualaLumpur, Malaysia
[g] Departments of Biomaterials & Applied Oral Sciences and Dental Clinical Science, Faculty of Dentistry, Dalhousie University, 5981 University Ave, Halifax, NS, B3H 1W2, Canada
[h] School of Biomedical Engineering (SBME), Faculty of Medicine, Dalhousie University, 5981 University Ave, Halifax, NS, B3H 1W2, Canada
[i] Faculty of Dental Medicine and Oral Health Sciences-McGill University, 2001 Av. McGill College, Montreal, QC, H3A 1G1, Canada
[j] Faculty of Dentistry, University of Toronto, 101 Elm St, Toronto, ON, M5G 2L3, Canada
[k] Dental Materials Science, Applied Oral Sciences & Community Dental Care, Faculty of Dentistry, The University of Hong Kong, 34 Hospital Road, Sai Ying Pun, Hong Kong Special Administrative Region

ARTICLE INFO

Keywords:
Bone
Collagen
Antimicrobial
Tri-calcium phosphate
Raman
Cytotoxicity

ABSTRACT

This paper describes a promising candidate molecule, investigates the pattern of scaffold composition which arises and assesses the effect of the agent on its mechanical properties.

Methods: Scaffold samples were fabricated using a commercial extrusion bioprinter equipped with a pneumatic printhead fitted with a 21G conical nozzle. The Pore Printability Index, and the area and perimeter of the pore within the grid patterns were quantified using ImageJ software (NIH, USA). Mechanical properties of scaffolds were assessed using atomic force microscopy. The phase composition and crystal structures were analyzed using X-ray diffraction and Raman mapping. Morphologies of human gingival fibroblastic cells were examined using scanning electron microscopy. Lactobacillus biofilms were generated for cytolysin peptide cleavage. A rabbit bone defect model with scaffold implantations was used to provide histologic specimens for measuring percentages of bone trabeculae, collagen fibers and inflammatory cells along with granulation tissue. The Primeway Total RNA Extraction Kit was used for RNA extraction.

Results: All bioink formulations demonstrated successful printing of 3D grid and solid square patterned scaffolds achieving Pr values exceeding 0.9. $_{0.1\ \%}$**K21** group showed the highest elastic modulus. XRD revealed a pattern producing around 90 % β-tricalcium phosphate displaying two peaks at 2θ angles. 0.1 % K21 and $_{0.1\ \%}$**CHX** did not alter scaffold's pore size and porosity. $_{0.1\ \%}$**K21** group exhibited highest ratio (62.5 ± 6.1 θ), significantly surpassing control. Surface morphologies of cells were also well retained. TEM image shows a sequence of structural changes in fibroblastic cell structure when exposed to K21. 0.1 % K21 proved to be critical in

Peer review under responsibility of the Japanese Society for Regenerative Medicine.

* Corresponding author. Applied Oral Sciences & Dental Clinical Sciences, Faculty of Dentistry, Dalhousie University, 5981 University Ave, Halifax, Nova Scotia, B3H 1W2, Canada.

** Corresponding author. Restorative Dentistry Division, School of Dentistry, International Medical University Kuala Lumpur, 126, Jalan Jalil Perkasa 19, Bukit Jalil, 57000, Wilayah Persekutuan Kuala Lumpur, Malaysia

E-mail address: umerdaood@imu.edu.my (U. Daood).

https://doi.org/10.1016/j.reth.2025.08.001
Received 18 June 2025; Received in revised form 31 July 2025; Accepted 2 August 2025

completely eradicating the biofilm. $_{0.}$**K21** group closed the openings of wound areas completely. Correlation coefficient of gene expression levels demonstrates sample variations and recurring instances among groupings. *Conclusion:* 3D-printing technologies with $_{0.1\ \%}$**K21** represent a significant advancement over conventional regenerative medicine techniques for bone-related treatments.

1. Introduction

3D printing, which is also referred to as rapid prototyping (RP) or additive manufacturing (AM), is the process of meticulously assembling layers of material to create a structure [1]. In medicine and dentistry, 3D printing has numerous clinical applications. Digital light processing (DLP), selective laser sintering (SLS), fused deposition modelling (FDM), and stereolithography (SLA) are among the most prevalent methods of 3D printing in dentistry. 3D printing's pivotal role lies in synthesizing customized scaffolds for bone regeneration [2]. Tissue engineering scaffolds aim to provide a conducive microenvironment for targeted cells, and the contemporary trend involves crafting tailored scaffolds with predetermined shapes, structures, and functions for optimal tissue regeneration [3]. Among various methodologies, 3D printing stands out, as its macro-microstructure effectively emulates the multi-scale architecture found in human body tissues [4]. Moreover, scaffolds that are generated using specific 3D printing techniques are exceptional delivery vehicles for molecules, facilitating the localised and sustained release of medications and/or biomolecules [5,6].

The periodontium consists of both soft and hard tissues, with alveolar bone playing a crucial role in tooth formation and tooth support in both maxilla and mandible. Alveolar bone forms during tooth eruption to establish osseous attachments to the periodontal ligament and disappears upon tooth loss [7]. Periodontal disease leads to localized bone loss regulated by systemic and local factors, primarily through bone resorption, eventually causing attachment loss and tooth loss. The bone loss induced by periodontitis manifests as osseous defects, either singularly or in various combinations [7]. Periodontal regenerative therapy is a dependable procedure when executed effectively. Nevertheless, its success is contingent upon a comprehensive analysis of etiological and contributing factors, cautious case selection, and an accurate diagnosis [8]. In periodontal disease, gram-negative anaerobic bacteria in dental plaque, such as Aggregatibacter actinomycetemcomitans and Porphyromonas gingivalis, are the primary contributors to oral health decline. These bacteria release toxins that directly damage periodontal tissues and initiate an inflammatory response. This inflammation triggers the release of cytokines, which activate osteoclasts—cells responsible for bone resorption. Understanding this interaction between bacterial pathogens, inflammation, and bone resorption is key to comprehending the progression of periodontal disease [9].

Tricalcium phosphate (TCP, Ca3(PO4)2), also known as calcium phosphate or tribasic calcium phosphate, exhibits three crystalline forms: alpha (α), beta (β), and gamma (γ) [10–13]. Composed of calcium ions (Ca 2+) and orthophosphate (PO4 3-), TCP closely resembles the hydroxyapatite structure ($Ca_{10}(PO_4)6(OH)_2$) yet has a different stoichiometry in its formula. Beta tricalcium phosphate exhibits a rhombohedral shape, while α and ά-tricalcium phosphate possess monoclinic and hexagonal structures, respectively. All polymorphs of tricalcium phosphate feature complex structures, consisting of tetrahedral phosphate connections with oxygen and calcium ions [14]. With regard to an active agent in this study, a Quaternary Ammonium Silane, (QAS), compound, codenamed K21, is a class of contact-killing biocidal polymer, that falls under the umbrella of quaternary ammonium compounds. Quaternary ammonium compounds are a category of biocides; this class of polymers depends on the covalent bonding of antimicrobial functional groups to the surface of the substance. K21 is a novel biomaterial of that type synthesised via a sol-gel technique, demonstrating a wide range of antibacterial properties and minimal cytotoxicity [15].

The action mode of QAS against bacterial cells entails the rupture of lipid bilayer membranes that comprise both the bacterial cytoplasmic membrane and the outer membrane of Gram-negative bacteria. The potent antimicrobial efficacy of QAS arises from its –C18H37 lipophilic alkyl chain, which penetrates bacterial cell membranes inflicting damage, and its positively charged nitrogen atoms, which are drawn to bacterial membranes containing negatively charged lipid moieties such as cardiolipin and phosphatidylglycerol [16]. The mechanism of K21 activity at the molecular level entails a positively charged quaternary nitrogen interacting with phospholipid acids in the membrane, while the hydrophobic tail infiltrates the hydrophilic core of the membrane. Exposure to K21 elevates surface pressure and induces a transition of the membrane from a liquid to a liquid crystalline state, leading to the creation of voids in the cell membranes, which results in membrane damage and cellular leakage. The most significant biocidal action is observed in quaternary ammonium compounds (QAS) with carbon chains of 10–12 atoms; deviations in chain length from this range reduce antibacterial efficacy. Research indicates that the optimal biocidal efficacy of quaternary ammonium compounds (QAS) against Gram-positive bacteria occurs with carbon chains of 12–14, but for Gram-negative bacteria, it is most effective with carbon chains of 14–16 [15].

Furthermore, QAS exhibits anti-inflammatory properties and promotes wound healing. Macrophages are a subset of mononuclear cells within the innate immune system that engulf bacteria and release proinflammatory and antimicrobial mediators. The M1 phenotype generates proinflammatory cytokines [IL-1, IL-6, (TNF)-α], whereas the M2 phenotype encompasses anti-inflammatory chemicals. M1 cells participate in initial reactions, while M2 cells are engaged in later inflammatory and tissue remodelling phases [17]. 0.5 % K21 significantly improves wound-healing activity, resulting in no observable wound area at 24 h compared to the control [18]. QAS provides an innovative biomaterial for the repair and regeneration of dental tissues. Consequently, the quest may be being completed for an agent that displays antibacterial and osteoblastic activities in a new heterogenous scaffold. Characterisation of the pattern of composition with the incorporated agent and its impact on the mechanical properties of this scaffold would be of great interest. Therefore, the null hypotheses tested were: (i) no antibacterial activities of the new composite scaffolds are observed, (ii) there is an absence of any incidence of osteoblastic activities promoted by the new composite scaffolds, and (iii) there are no observed mechanical property changes of the composite scaffold as determined by performing standard characterization procedures.

2. Materials and methods

The Institutional Research Ethical Committee approved the project (4.12/JCM-285/2024).

2.1. Bioink preparation

The bioink used in this study was commercially available, Cellink Bone (CELLINK, Sweden), and was composed of nano fibrillated cellulose, alginate, and tricalcium phosphate particles. Three groups of bioink were prepared. Cellink Bone mixed with 10 % (v/v) distilled water served as control group and those mixed with 10 % (v/v) $_{0.1\ \%}$**K21** or 10 % (v/v) $_{0.1\ \%}$**CHX** (CHX) served as antimicrobial groups.

For each group, 100 μL of distilled water, CHX, or K21 solution was added to 900 μL of Cellink Bone. The mixture was homogenised using a syringe-to-syringe mixing method to ensure uniform distribution of

components and transferred into a 3 mL bioprinting cartridge (CELLINK).

2.2. A3D printing of scaffolds

The scaffolds were fabricated using a commercial extrusion bioprinter (Cellink BioX, CELLINK) equipped with a pneumatic printhead and fitted with a 21G conical nozzle. The bioprinting process was performed under sterile conditions using optimized printing pressure (13–15 kPa) and speed (10–15 mm/s). The prepared bioinks were bioprinted as 3D grid or solid pattern scaffolds with three stacked layers to create structures with overall dimensions of 1.5 cm × 1.5 cm x 0.5 cm. For the solid scaffolds, a rectilinear infill pattern was used, wherein the infill pattern for layer 2 was designed to be at right angle to the orientation in layers 1 and 3. Following bioprinting, the scaffolds were immersed in a calcium-based ionic crosslinking solution (CELLINK Crosslinking Agent) for 2 min to stabilize the hydrogel matrix. The scaffolds were then washed with sterile phosphate-buffered saline (PBS) to remove excess crosslinking agent. After washing, the scaffolds were freeze-dried using a lyophilizer for 48 h to remove moisture and enhance their structural stability.

To assess the shape fidelity of the 3D printed structures, the Pore Printability Index (Pr), pore area and perimeter of the pore within the grid patterns were quantified using ImageJ software (NIH, USA) as previously described [19]. The Pr was calculated based on Equation (1). A Pr value greater than 0.8 was considered indicative of excellent shape fidelity.

$$\mathrm{Pr} = \frac{(\textit{Perimeter of the pores})^2}{(\textit{Area of the pores} \times 16)} \quad [1]$$

2.3. Atomic force microscopy (AFM)

To evaluate the mechanical properties of the scaffolds, Atomic Force Microscopy (AFM) was employed (n = 5 specimens per group unless specified otherwise) in Tapping Mode (Multimode/AFM, NanoScope IV, Bruker Instruments) utilising a silicon nitride probe (NP–S, Bruker) with a nominal tip radius of 10 nm, operating at a resonance frequency of 18–24 KHz and a spring constant of 0.06–0.12 N/m. The oscillating probe in Tapping Mode maps the topography of the scaffolds, with the cantilever's oscillation amplitude changing with sample surface topography. Load relaxation tests were conducted in which the peak displacement was maintained while the load was measured. Indentations were conducted at the identical sample location, permitting adequate time for the specimens to recuperate. The hardness value of the specimens i.e. the elastic modulus and hardness values were obtained and calculated for the mean value. The final values were determined by using means and dividing by standard deviations (SD) to the means and multiplying the results by 100 so they could be later subjected to statistical analysis.

2.4. Xray diffraction analysis (XRD)

The phase compositions and crystal structures of the synthesised scaffolds were examined via X-ray diffraction (XRD: GNR, APD 2000, PRO) throughout a 2θ range of 20–60° with a radiation wavelength of 1.54 Å. The crystalline phases of hydroxyapatite and beta-tricalcium phosphate were validated using JCPDS cards No. 09–0432 and No. 09–0169, respectively.

2.5. Porosity analysis (PA)

The porosity of the scaffolds was assessed utilising the liquid displacement method. Small discs were excised from the scaffolds and measured for weight. Each scaffold disc, after being weighed, was submerged in a predetermined volume of ethanol (V1) for 1 h within a falcon tube. The amount of ethanol containing the sample after 1 h was noted as (V2). Upon the extraction of the sample, the residual volume of ethanol was quantified as (V3). The porosity was subsequently determined using the following equation:

$$\text{Porosity } (\%) = V1 - V3V2 - V3 \text{ x } 100\%$$

2.6. Raman imaging and mapping

Raman imaging and mapping were conducted with two distinct Raman spectrometers.

2.6.1. Raman mapping

Raman spectra were obtained using a DXR Raman Microscope (Thermo Scientific, Waltham, MA, USA), which employed a 780-nm laser with an output of 13 mW to collect and capture clear signals from both the mineral and organic compounds found within the scaffolds. The spectra obtained were recorded with reference to the 200-2600cm-1 range with a spectral resolution of 4 cm^{-1} and a 25-pinhole aperture. For data collection, an exposure time of 6 s was set, with 10 times repetition, using a 10x objective. The microscope was equipped with a 0.8-megapixel CCD Camera (Sentech, Ebina, Kanagawa, Japan). During the mapping process, 875 measurements were taken with a 25 μm step size, using a 10x objective and autofocus at each point, due to the variations in sample size.

2.6.2. Raman imaging

Raman imaging and depth profiles were obtained utilising the inVia™ Confocal Raman Microscope (Renishaw, UK), which is outfitted with a Newton 970 EMCCD detection camera (Andor, Belfast, Northern Ireland, UK) and a 20x long-distance objective (Olympus Plan N NA = 0.25, Olympus, Shinjuku, Tokyo, Japan). Data collection utilised a 633 nm He–Ne laser (RL633 HeNe Laser, Renishaw, Wotton-under-Edge, Gloucestershire, UK) with a maximum power of 25 mW at the sample.

2.7. Scanning electron microscopy (SEM) and transmission electron microscopy of fibroblastic cells

The morphology and size of the printed scaffolds were analyzed via scanning electron microscopy (Auriga Compact, Zeiss, Germany) at an accelerating voltage of 10 kV. The specimens underwent sputter-coating with gold for 10 s at a vacuum pressure of 80 mTorr.

The human gingival fibroblasts (ATCC; HGF, PCS-201−018, ATCC, USA) were cultured at 37 ± 2 °C in a humidified environment (5 % CO2). Upon attaining 60–80 % confluency, cells were detached from the flask surface utilising 0.05 % trypsin. Cells were centrifuged for 12 min and subsequently inoculated into flasks at 8 °C, after which experimental scaffolds were added for 24 h. The cell morphologies on the scaffolds were analyzed using a high-resolution field emission scanning electron microscope (Auriga Compact, Zeiss, Germany) at an accelerating voltage of 10 kV. Before conducting scanning electron microscopy (SEM) tests, all specimens underwent sputter-coating with palladium ion sputtering (EMACE600, Leica, Germany). The scaffolds were then stabilised using a 4 % glutaraldehyde solution in PBS for 4 h at ambient temperature.

The $_{0.1\ \%}$**K21** solution was administered to grow cells for 48 h. The cells were examined via high-resolution transmission electron microscopy (JEOL 3010 TEM, JEOL USA, Peabody, MA) at an accelerating voltage of 200 kV at various time intervals (1 h, 6 h, 12 h, 24 h, 36 h, and 48 h).

2.8. Cytolysins

2.8.1. Preparation of acyl-homoserine lactones (AHLs) to enhance E faecalis virulence

The acyl-homoserine lactones employed in this study were *N*-

Butyryl-DL-homoserine lactone (Sigma-Aldrich, Merck KGaA, MY), *N*-Hexanoyl- L-homoserine lactone (Sigma-Aldrich, Merck KGaA, MY), and *N*-Octanoyl-L-homoserine lactone (Sigma-Aldrich, Merck KGaA, MY). The biofilms were generated with *E. faecalis* (#29212, ATCC Manassas, VI) inside 24-well polystyrene plates (Sarstedt AG & Co. KG, Nümbrecht, DE).

The utilised AHLs were of short acyl chain length. The short-chain group comprised C4-HSL, OC4-HSL, C6-HSL, OC6-HSL, and C8-HSL. All AHLs were diluted to a concentration of 1 mg/mL and kept at −20 °C. Before each experiment, intermediate dilutions of the stock solutions were produced in sterile water to create mixtures of the individual short-chain AHLs, achieving a total concentration of 20 μM for each AHL.

Biofilms were cultivated on the bottoms of 24-well polystyrene plates (Sarstedt AG & Co. KG, Nümbrecht, DE). To do this, each well was filled with 1.7 mL of BHI broth, followed by the addition of 200 μL of the OD-adjusted E. faecalis (#29212, ATCC Manassas, VI) suspension to each well. One hundred microlitres of the short- or long-chain AHL mixtures were subsequently added to the respective wells, resulting in a working concentration of 1 μM for each individual AHL in the mixture (acetonitrile fractions ranging from 0.1 to 0.5 % v/v). After biofilm incubation, the culture medium were aspirated, and the biofilms were rinsed three times with a phosphate-buffered saline (PBS) solution. All wells were subsequently stained for 20 min in 2 mL of a 0.04 % crystal violet (CV) solution (Sigma-Aldrich). Following staining, the surplus dye was extracted using aspiration, and the biofilms were subsequently rinsed three times with PBS. The dyed biofilms were homogenised in 2 mL of 33 % acetic acid, and the incorporated CV in the biomass was quantified at 595 nm.

2.8.2. Cytolysin peptide cleavage

Recombinant Cytolysin A protease was produced and subsequently purified (data not presented). The peptide solution was thawed and incubated with 100 μL of CylA (0.1 mg/mL) overnight at room temperature. The peptide solution was acidified with 2 % trifluoroacetic acid (TFA), centrifuged at 4500×*g* for 10 min, filtered through a 0.45 μm PVDF syringe filter, and then purified using HPLC. The employed treatments included **$_{0.1\ \%}$K21** scaffold, 1 % K21 solution, **$_{0.1\ \%}$CHX** scaffold, 1 % CHX solution, and control groups.

2.9. Antibacterial activity

2.9.1. Biofilm preparation

Porphyromonas gingivalis was utilised in Brain Heart Infusion (BHI) broth sourced from Difco Laboratories, Detroit, MI, USA, for biofilm formation. The bacterial suspension was calibrated to a 1.5 McFarland turbidity standard. The bacteria were first cultivated on blood agar plates in anaerobic conditions at 37 °C for 20 h. The bacteria were subsequently inoculated into BHI broth enriched with 8 % sucrose (pH 7.4) and varying doses of xylitol (0–2 %), followed by incubation at 37 °C for 48 h. Following incubation, the bacterial cells were harvested via centrifugation at 4000 rpm for 15 min, and the cell pellets were rinsed three times with phosphate-buffered saline (PBS, 0.01 M, pH 7.2). The cells were subsequently resuspended in 100 ml of growth medium and calibrated to a McFarland standard number 3, corresponding to a concentration of 10^9 cells/mL. Utilising sterilised syringes, 5 ml of the BHI broth and bacterial inoculum mixture were employed to fill the canals, which were subsequently cultured for three days to facilitate biofilm formation. After this interval, permitting bacterial growth for an additional seven days.

2.10. Establishment of rabbit bone defect model and scaffold implantation

2.10.1. Preoperative preparation

An experimental study was designed incorporating 27 (2-month-old) rabbits of either gender, weighing 1–2 kg, which were habituated to soft food for a minimum of seven days before surgery. Rabbits were divided into 3 main groups of 9 each. The experimental groups comprised of.

- Group A (Surgical defect was created, 3D-Collagen bone mesh was placed in the defect, and sutured)
- Group B (Surgical defect was created, and 3D-Collagen bone mesh with 0.1 % k21 was placed in the defect and then sutured)
- Group C (Surgical defect was created and 3D-Collagen bone mesh with chlorhexidine was placed in the defect and then sutured).

Surgical equipment and gauze were sterilised using an autoclave. Buprenorphine at a dosage of 0.02–0.03 mg/kg was subcutaneously delivered to each animal in the scapular region, utilising a 25-gauge needle and a suitably sized syringe for analgesia. The operation table was sanitised using 70 % (vol/vol) ethanol. Xylazine at a dosage of 5–9 mg/kg and Ketamine at 30–35 mg/kg were injected intramuscularly for induction. Xylazine was administered first, followed by a period of approximately 1–2 min before administering Ketamine. The injections were performed on the quadriceps of each side using a 25-gauge needle and a suitably sized syringe. The profundity of anaesthesia was confirmed by the absence of reflexive response to toe pinching.

2.10.2. Operative procedure

Each animal was placed on an operating table in the dorsal position, its mouth was opened with the help of custom-made elevators, and the right maxilla was exposed by retracting the upper lip adjacent to the anterior diastema (between incisors and premolars). An incision was made using a scalpel with a no. 15 blade at the distal gingival margin of right maxillary incisor on the alveolar ridge in an anterior to posterior manner. The flap was elevated with the periosteal elevator to expose the periosteum on buccal side of the incision. The sloped curve of the incisor was visible and functioned as a landmark for the creation of the defect. A surgical tungsten carbide bur with round head (head size-2 mm length 44 mm) on slow speed motor was used to create a partial thickness defect (2 × 2 mm) in bone. Continuous irrigation with saline was provided during the procedure. The bur was centered on the intended area and root of the incisor along with periodontal ligament was secured for continuous provision of regenerating cells. The scaffold was placed in the defect and the incision was approximated using 4-0 surgical silk sutures.

2.10.3. Postoperative care

The incision was cleaned with the warm saline to remove blood. 0.5 mg/kg of 0.25 % bupivacaine was administered intradermally along the incision site with a 25-gauge needle and appropriately sized syringe. When the animal had maintained the sternal recumbency, it was returned to animal housing. A postoperative analgesia regimen was administered (0.02–0.03 mg/kg buprenorphine subcutaneously every 12 h for 48 h. Rabbits were fed on regular rabbit chow soaked in water and mixed with apple sauce.

2.10.4. Euthanasia and 3D graft/bone collection

At day 14, day 21 and day 28, the animals were euthanized in a chloroform chamber, and then a maxillary dissection was performed for histological evaluation [20].

2.10.5. Histological staining and evaluation

For histologic examination, specimens were decalcified for 4–5 days and coronal sections of 5 μm were cut and stained with haematoxylin and eosin. The following parameters were studied in these histological sections to evaluate healing and regeneration.

2.10.6. Measuring percentage of bone trabeculae

Histomorphometric analysis was conducted for each histological section. The entire defect area (2 × 2 mm) at the power of (4x10 = 40x) was analyzed to calculate the percentage of bone trabeculae within it,

rather than just selected fields. The "mean value was taken at this magnification for analysis of the entire defect. 3 sections on the same slide were analyzed per animal. The proportion of the area occupied by bone trabeculae was assessed utilising ImageJ, version 1.54g. The average value was recorded at a magnification of 40X. The subsequent data analysis was predicated on the mean % computed for each group [21].

1. **The number of inflammatory cells**: Inflammatory cells (neutrophils and macrophages) were observed in the haematoxylin and eosin-stained sections under the microscope at 40X and 100X. Scoring was done as follows (Aydinyurt et al., 2020);
   I. Score 0 = No inflammatory cell
   II. Score 1 = 1–5 inflammatory cells
   III. Score 2 = 6–9 inflammatory cells
   IV. Score 3 = 10≤ inflammatory cells
2. **Collagen fiber bundles arrangement**: Collagen fiber bundles from were evaluated for their organization. Scoring was done according to the following criteria [22].
   I. Disrupted = 0
   II. Organized = 1
3. **Amount of granulation tissue** [20]
   I. Absent-0
   II. Scanty-1
   III. Moderate −2
   IV. Profound −3

2.10.7. Cell culture and biocompatibility evaluation of scaffolds

The 3T3 cells (ATCC CRL-658) (passage 5–7) were cultured in 60 mm cell culture dishes with a seeding density of 0.6×10^7 cells per dish using complete DMEM media (10 % FBS and 1 % Penicillin-Streptomycin). The cells were incubated in a 37 °C, 5 % CO_2 humidified atmosphere for 24 h. The cells were then treated with K21 at 0.00025 % (13.58 nM) in a mixture of ethanol and DMEM medium and were incubated for another 24 h. The cells were harvested at the density of 1×10^7 cells.

2.11. RNA extraction

The Primeway Total RNA Extraction Kit was used for RNA extraction, and the steps were performed following the manufacturer's instructions. The cell lysis was initiated by using the mixture of TR buffer (700 μL) and 2-Mercaptoethanol (7 μL) per 1×10^7 cells. The cells were homogenised by using a 20-gauge needle fitted with 1 mL RNase-free syringe. The lysate was passed through the needle at least five times or until homogenous. The homogenised cell lysate was transferred into the PrimeWay Filter Column fitted in a new collection tube, and the contents were centrifuged at 12,000×*g* for 1 min. The flow-through was collected while the PrimeWay Filter Column was discarded. Absolute ethanol (300 μL) was added to the flow-through and the contents were mixed by pipetting. The contents were transferred into a PrimeWay RNA Column placed in a new collecting tube. The samples were centrifuged at 12,000×*g* for 1 min. The effluent was disposed of. Seven hundred microlitres of wash buffer R1 was added to the PrimWay RNA Column, and the mixture was centrifuged at 12,000×*g* for 1 min. The effluent was disposed of. Five microlitres of DNase 1 solution (2 U/μL) and 45 μL of DNase 1 buffer were introduced into the centre of the column. The column was incubated for 15 min at ambient temperature. Five hundred microlitres of wash buffer R1 were added to the column, and the mixture was centrifuged at 12,000×*g* for 1 min. The effluent was disposed of. Five hundred microlitres of wash buffer R2 were added to the column, and the mixture was centrifuged at 12,000×*g* for 1 min. The effluent was disposed of. The column underwent centrifugation at 12,000×*g* for 2 min to desiccate the membrane. RNase-free water (80 μL) was introduced to the column, and the mixture was incubated for 2 min at ambient temperature. The samples were centrifuged at 12,000×*g* for 2 min to extract the total RNA.

3. Results

Fig. 1 illustrates the schematic depiction of the experiments conducted in this study.

3.1. Fabrication of 3D printed composite scaffolds

All three bioink formulations for control (Cellink Bone with distilled water), and antimicrobial groups (Cellink Bone with K21 or CHX) demonstrated successful printing of 3D grid and solid square patterned scaffolds. The printed structures maintained the designed geometry (Fig. 2A and B, Supplementary Video SV1, SV2). The Pore Printability Index (Pr), a measure of shape fidelity, was quantified for the 3D grid patterned scaffolds (Fig. 2C). All three bioinks achieved Pr values exceeding 0.9, indicating excellent shape fidelity and the capability of the printer to reproduce the desired pore architecture. This indicates that the bioinks, regardless of the presence or type of antimicrobial compounds were capable of consistently reproducing the architecture.

3.2. Atomic Force Microscopy

Table 1 represents the elastic modulus (GPa), hardness (GPa), compressive strength (MPa) with measured porosity (%) of scaffolds of all experimental groups. It was observed that the **$_{0.1\ \%}$K21** group showed the highest elastic modulus at 1.98+-0.09 GPa, the highest compressive strength at 1.41+-0.05 Mpa and the highest measured porosity at 86+-2.3 %. Additionally, data reveals that **$_{0.1\ \%}$CHX** group has the highest hardness at 2.3+-0.4 GPa.

3.3. XRD analysis

Fig. 3 depicts the XRD pattern for the scaffolds (n = 5) at ambient temperature. For pictorial representation, patterns are discernible solely between the 8–62° range on the 2θ scale. All samples were phase-identified across a complete range from 5 to 80°.The findings revealed a pattern producing around 90 % TCP with β-tricalcium phosphate. β-tricalcium phosphate, indicated by the red arrow, displays two significant peaks at 2θ angles of 27.25° and 29.27°. Phosphate planes were found in all samples at (211) and (112) (ICDD card No. 00-004-0829).

3.4. Porosity analysis

The surfaces of these scaffolds (Table 1) exhibit a morphology of homogenous structure containing spherical pores. The addition of antimicrobials **$_{0.1\ \%}$K21** and **$_{0.1\ \%}$CHX** did not significantly alter the scaffold's pore size and porosity. However, the scaffold geometry of 0.1 % antimicrobial K21 appears to be more consistent and has a thicker strut thickness, while the control and the **$_{0.1\ \%}$CHX** scaffolds appeared to have scaffold geometry consisting of randomized arrangements and thinner strut thicknesses. Note that this analysis also shows that the scaffold with **$_{0.1\ \%}$K21** achieved scaffold macrostructure and geometry homogeneity across all surfaces.

3.5. Raman imaging/mapping

Fig. 4 represents micro-Raman spectra obtained from the phosphate vibrational modes (ν_1 PO_4^{3-}) found on the scaffolds across all experimental groups; **$_{0.1\ \%}$K21**, **$_{0.1\ \%}$CHX**, and control. The relative distribution of the primary elements of calcium and phosphorus of control and experimental groups indicated the measurement position whereby the main components of the scaffolds represented crystalline hydroxyapatite in highly ordered crystalline structures which are appear highly mineralized based on the data for the groups. Similarly, the spectra of scaffolds were primarily characterized by the two main Raman-active vibrational modes of PO_4^{3-} at 960 cm^{-1}. The symmetric ν_1 P–O stretching band was observed at 960 cm^{-1}, while the asymmetric ν_3 P–O

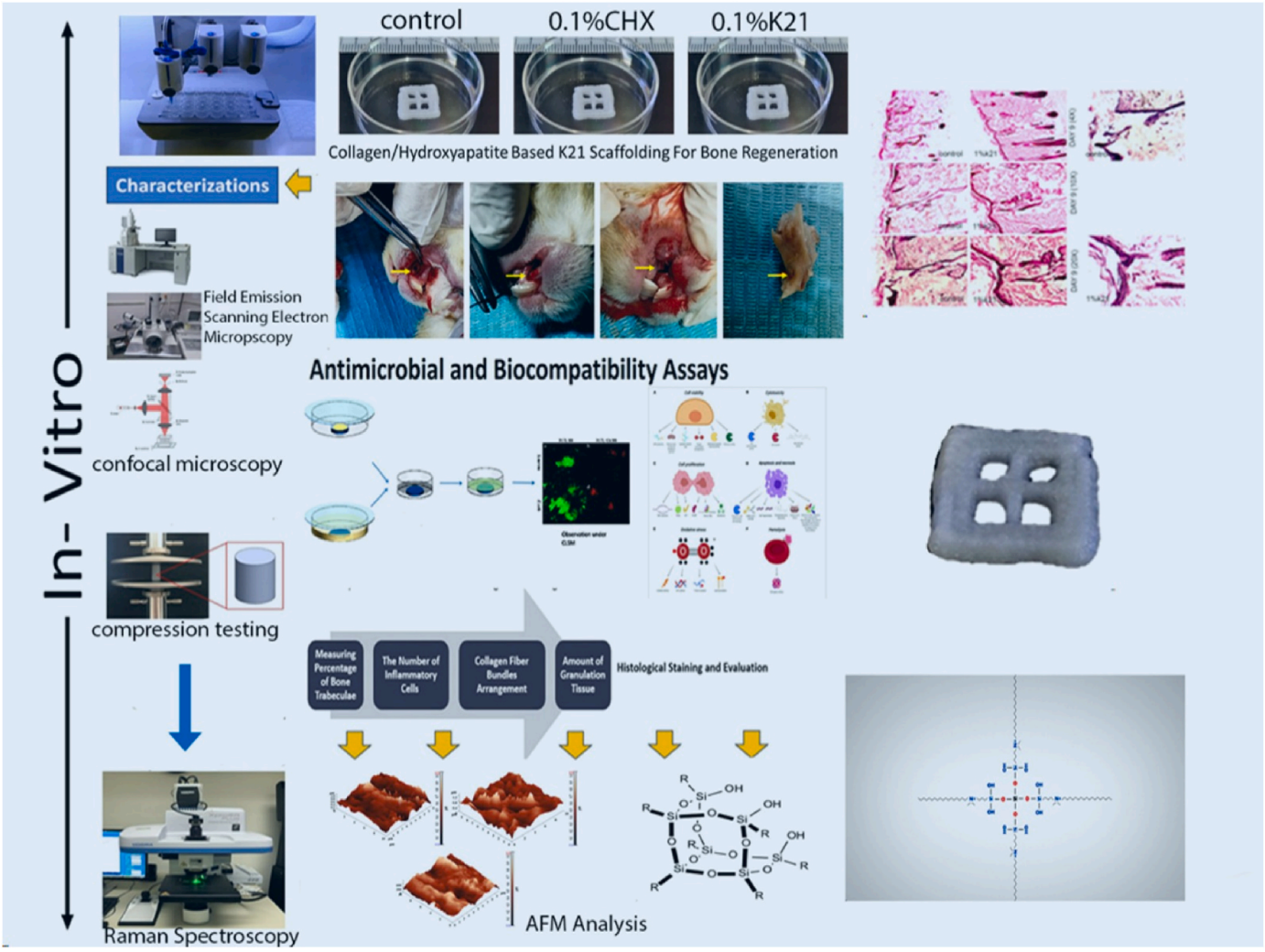

Fig. 1. Schematic representation of experimental evaluation of 3D printed scaffolds study.

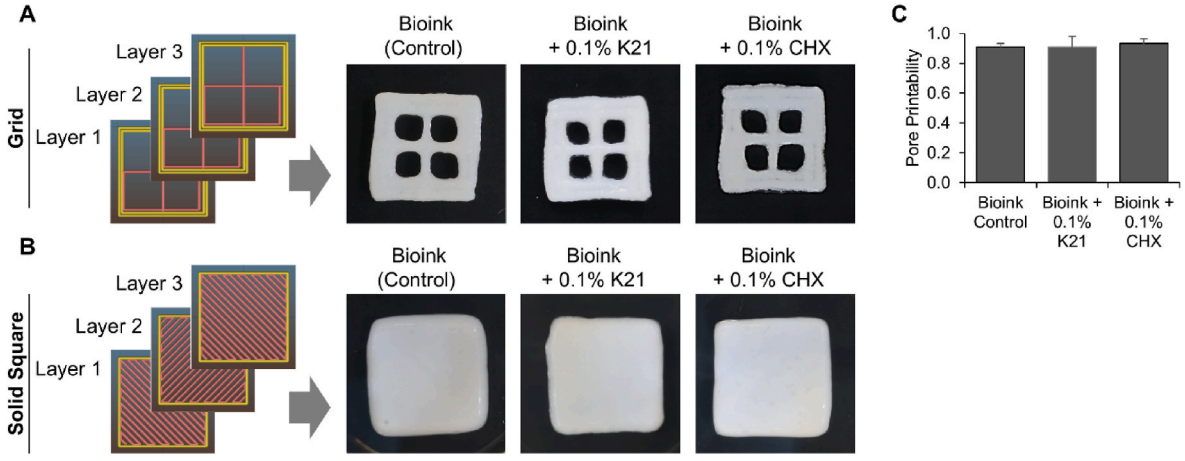

Fig. 2. 3D printed scaffolds and shape fidelity. Representative 3D design and images of 3D printed (A) grid and (B) solid square patterned scaffolds fabricated using the three bioinks - control (Cellink Bone with distilled water), Cellink Bone with K21, and Cellink Bone with chlorhexidine (CHX). (C) Quantification of pore printability index (Pr) for the scaffolds. Data are presented as mean ± standard deviation (n = 4).

stretching band appeared at 1045 cm^{-1} (red arrow). At 960 cm^{-1} peak, the **$_{0.1\ \%}$K21** group exhibits the highest intensity of the ν_1 PO_4^{3-} peak, indicating a greater degree of crystallinity and mineralization as compared to the other groups. In contrast, the **$_{0.1\ \%}$CHX** group demonstrated moderate peak intensity, suggesting some improvement in mineralization quality, but not to the same extent as the K21 group. The control group showed the lowest peak intensity, reflecting mineralization. In addition, the supporting microscopy images further

Table 1
Summary of data acquired for the mechanical property assessment of scaffold samples. The elastic modulus, hardness, and compressive strength of 3D-printed designs ($p < 0.05$) are shown as mean ± standard deviation for all mechanical attributes. Values denoted by distinct letters and numerals exhibit significant differences ($p < 0.05$).

Groups	Elastic Modulus (GPa)	Hardness (GPa)	Compressive Strength (MPa)	Measured Porosity (%)
Ct	1.1 ± 0.07 A	2.1 ± 0.8 a	0.92 ± 0.03 λ	83 ± 4.4 δ
0.1 %CHX	0.9 ± 0.04 A	2.3 ± 0.4 a	0.9 ± 0.06 λ	84 ± 6.2 δ
0.1 %K21	1.98 ± 0.09 B	2.2 ± 0.6 b	1.41 ± 0.05 θ	86 ± 2.3 φ

$p < 0.05$.

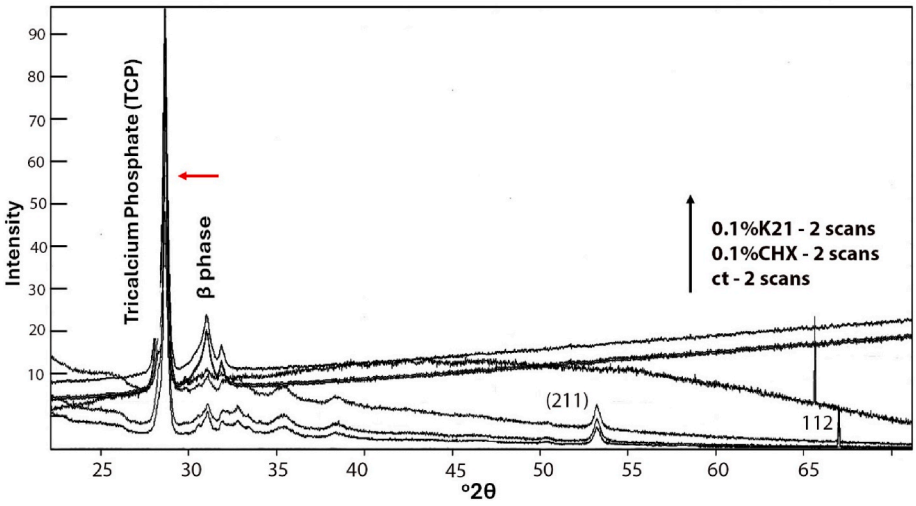

Fig. 3. The XRD figure illustrates the XRD pattern for the scaffolds at room temperature. For pictorial representation, patterns are discernible solely between the 8–62° range on the 2θ scale. All samples were phase-identified across the whole range of patterns from 5 to 80°.The findings revealed a pattern producing around 90 % TCP with β-tricalcium phosphate.

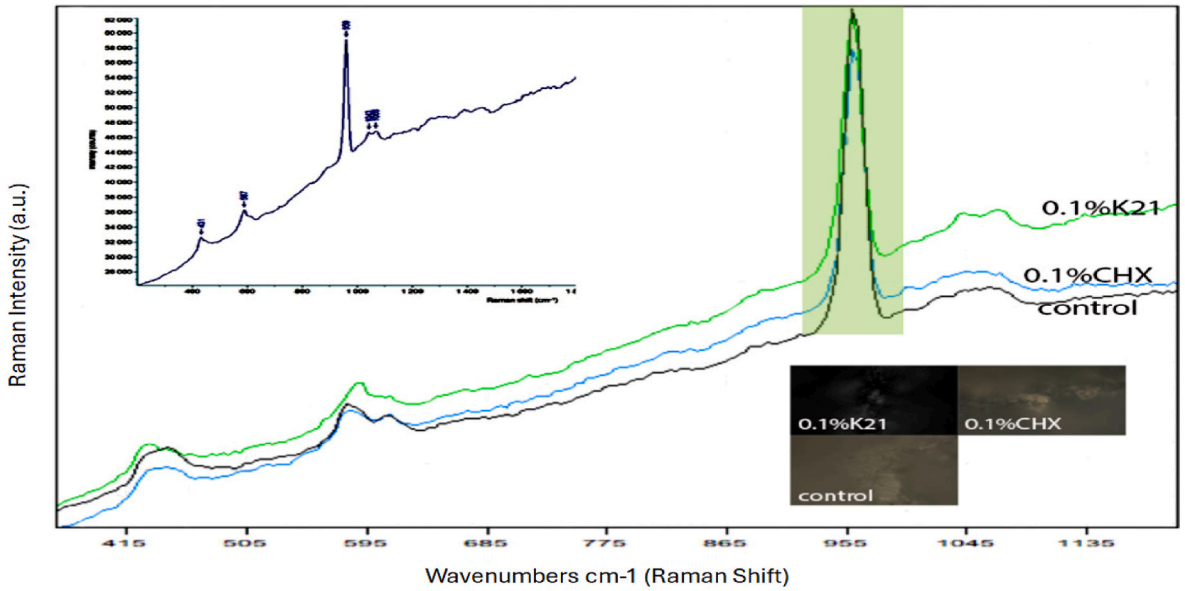

Fig. 4. Representative Raman Spectra of scaffold samples (**0.1 %K21**, **0.1 %CHX**, and control) showing phosphate vibrational mode (960 cm^{-1}). The relative distribution of the primary elements of calcium and phosphorus of control and experimental groups indicated the measurement position whereby the main components of the scaffolds represented crystalline hydroxyapatite in highly ordered crystalline structures which are highly mineralized based on the groups. Similarly, the spectra of scaffolds were primarily characterized by the two main Raman-active vibrational modes of PO_4^{3-} at 960 cm^{-1}.

corroborate these findings, as the **0.1 %K21** sample showed a denser and more uniform surface, as compared to **0.1 %CHX** and control groups, highlighting their potential as effective mineralization agents.

Table 2 displays the intensity of $v_1PO_4^{3-}$ (960 cm^{-1}) and $v_1CO_3^{2-}$ (1071 cm^{-1}), as well as the $v_1CO_3^{2-}/v_1PO_4^{3-}$ ratio, which elucidates the quality and composition of crystals in the presence of K21 and CHX. The carbonate-to-phosphate ratio was calculated based on the relevant vibrational intensities and multiplied by 1000 to facilitate

Table 2
Table of Raman intensities V1CO3 2-/V1PO4 3- ratio multiplied by 1000, calculated on three spectra of mean clusters for each sample.

Groups	$_{V1}PO_4^{3-}$ (960 cm^{-1}) Mean	$_{V1}CO_3^{2-}/_{V1}PO_4^{3-}$ ratio 1071/960 * 1000
Control	498 ± 6.5 A	49.3 ± 4.3 ʎ
0.1 %CHX	501 ± 11.1 A	53.4 ± 4.7 ʎ
0.1 %K21	463 ± 3.9 B	62.5 ± 6.1 θ

$p < 0.001$.

interpretation, given the differences in intensity ranges. Statistical analysis was performed using one-way ANOVA with significance set at $p < 0.001$. The control and **0.1 %CHX** groups showed similar $v_1PO_4^{3-}$ values (498 ± 6.5 A and 501 ± 11.1 A, respectively), reflecting relatively stable phosphate intensities. However, the **0.1 %K21** group demonstrated a significantly lower $v_1PO_4^{3-}$ intensity (463 ± 3.9 B), which may indicate a reorganization or modification of the phosphate structure. The 0.1 % K21 group exhibited the highest ratio (62.5 ± 6.1 θ), significantly surpassing the Control (49.3 ± 4.3 λ) and CHX (53.4 ± 4.7 λ) groups.

3.6. SEM and transmission electron microscopy of fibroblastic cells

The SEM morphology of printed scaffolds, both with K21 and CHX, at 2K magnifications is illustrated in Fig. 5. All scaffolds demonstrated evenly orientated channels and pores with micrometre resolution. The comparison of (Fig. 5B) 0.1 %CHX and (Fig. 5C) 0.1 %K21 top-view images of the scaffolds demonstrated that their shapes were well preserved with minimal morphological alterations. Surface morphologies were also well retained, and showed little evidence of significant structural rearrangement, as seen with the control groups (Fig. 5A).

In addition, the TEM image shows a sequence of structural changes in the fibroblastic cell structure (Fig. 6A) when exposed to the K21 molecule over time. Initially, the representative fibroblast shows no visible disruption or interaction with the external agent. The cell structure then begins to show localized changes as the K21 molecules are ingested in the first hour. The molecule then appears fragmented after 6 h, indicating K21 dispersion. The molecule is further degraded, after 36 h with effective breakdown and clearance of the K21 molecule seen after 48 h. The in vitro study was also conducted to investigate the viability of fibroblasts on the scaffolds using SEM (Fig. 6B–E). The SEM analysis revealed cell adhesion, growth and proliferation of fibroblasts on the scaffolds in both (Fig. 6C) 0.1 % chlorhexidine and (Fig. 6D) 0.1 %K21 groups, indicating the division of the living cells as compared to the control groups (Fig. 6A and B).

3.7. Cytolysin peptide cleavage

Biofilm virulence was significantly enhanced (Fig. 7) in the presence of AHLs ($p < 0.05$). However, this virulence was substantially reduced ($p < 0.05$) when exposed to **0.1 %K21** scaffolds, particularly at concentrations similar to those of **0.1 %CHX**. Notably, a 0.1 % concentration of K21 proved to be critical in completely eradicating the biofilm. Early evaluation of biofilm formation within the first four to 6 h revealed a 0 % optical density (OD) in 1 % solution K21-treated samples, indicating its rapid and effective action against biofilms.

3.8. Antibacterial evaluation

Fig. 8 illustrates fluorescence microscopy images representing the viability of Porphyromonas gingivalis in biofilms subjected to three treatments (Fig. 8B): control, **0.1 %CHX**, and **0.1 %K21**. In the control group, the biofilm primarily exhibits dense green fluorescence clusters with minimal red regions, indicating a high proportion of live bacterial cells and only a few dead cells. Biofilms treated with **0.1 %CHX** scaffolds display a mixed fluorescence pattern, with both green and red areas visible. The increased red fluorescence compared to the control suggests a notable reduction in the number of live bacteria. Finally, biofilms treated with **0.1 %K21** predominantly exhibit red fluorescence, signifying a high proportion of dead bacteria. The percentage of dead bacterial cells for each group are provided in the image table (Fig. 8A) compared by one-way ANOVA. The quantity of living bacteria in single species biofilms diminished dramatically with 0.1 % K21 scaffolds ($p < 0.05$).

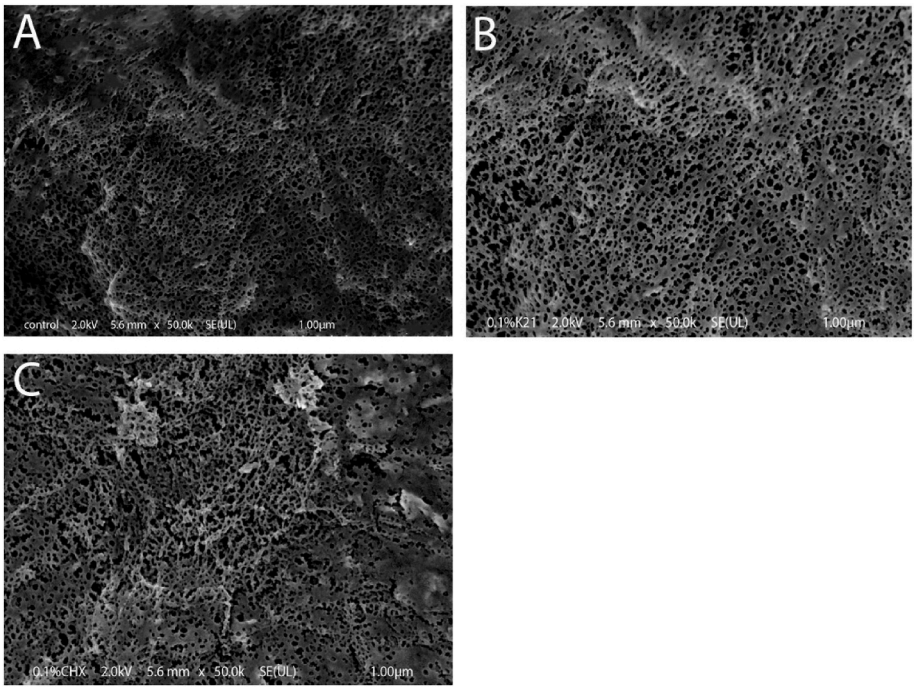

Fig. 5. Figure shows representative SEM images of scaffolds from each experimental group, labelled into groups of (A) control; (B) **0.1 %K21**; (C) **0.1 %CHX**. All scaffolds demonstrated evenly orientated channels and pores with micrometre resolution.

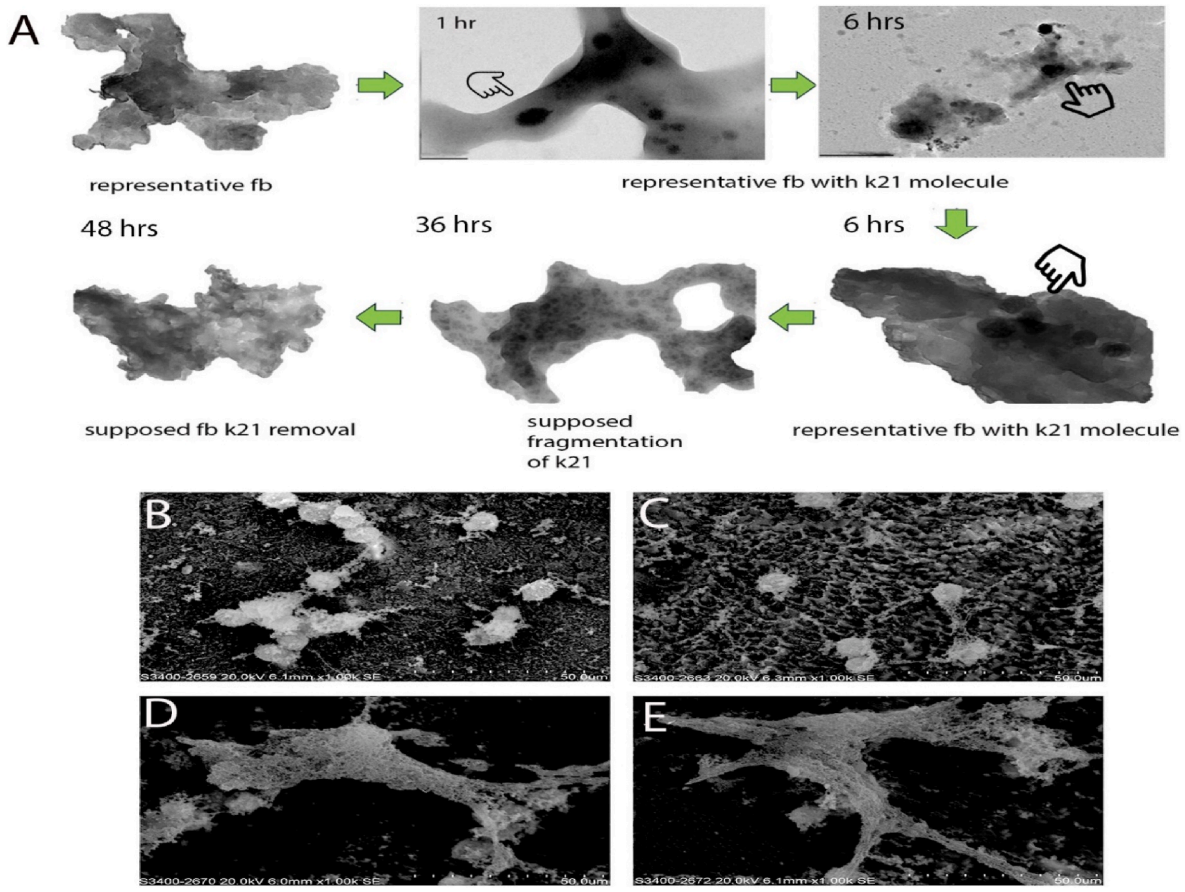

Fig. 6. (A) The TEM image shows a sequence of structural changes in the biofilm when exposed to the K21 molecule over time. (B–E) Illustrates scanning electron images representing the viability of fibroblasts on the scaffolds subjected to three different groups: (B–C) control, (D) 0.1 % chlorhexidine and (E) $_{0.1\ \%}$**K21**.

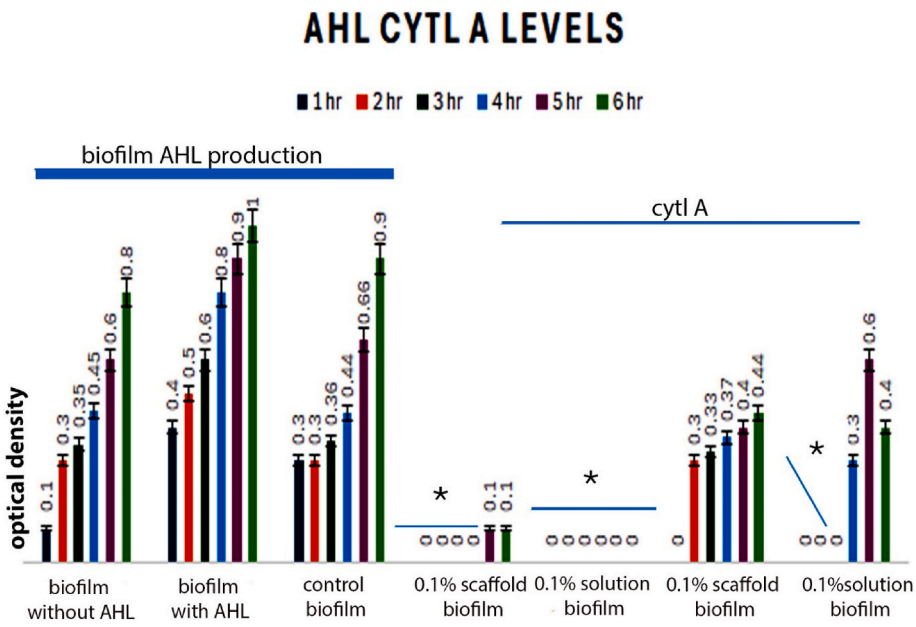

Fig. 7. Evaluation (optical density*) of biofilms and cytl A peptide over a period of 6 h in E Faecalis biofilm. Comparator CHX with similar concentration of 0.46 % and $_{0.1\ \%}$**CHX** is also shown ($p < 0.05$).

3.9. Bone defect model and scaffold implantation

For the in vivo experiment the animal defect model (Fig. 9a-d), was used to assess osteogenic potential of the scaffold. On day (Fig. 9 e-j) 14 (Fig. 9 k-p), day 21 and (Fig. 9 q-w) day 28, the animals were euthanized in chloroform chamber, a maxillary dissection was performed for histological evaluation. Specimens were decalcified for 4–5 days, then coronal sections of 5 μm were cut and stained with haematoxylin and

A

Groups	Live Percentage (%)	Dead Percentage (%)
Control	97.4±3.2 A	2.6±0.4 a
0.1%CHX	23.3±4.9 B	76.7±0.9 b
0.1%K21	3.9±5.5 C	96.1±1.1 c

B

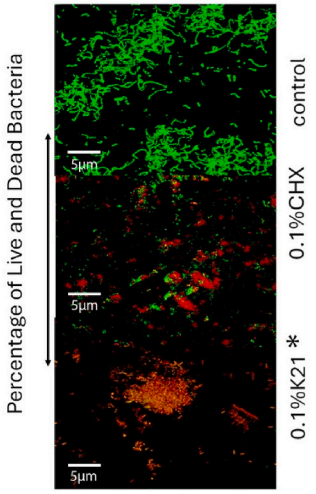

Fig. 8. Figure illustrates fluorescence microscopy images representing the viability of Porphyromonas gingivalis in biofilms subjected to three treatments: control, $_{0.1\ \%}$**CHX**, and $_{0.1\ \%}$**K21**. In the control group, the biofilm primarily exhibits dense green fluorescence clusters with minimal red regions. Biofilms treated with $_{0.1\ \%}$**CHX** scaffolds display a mixed fluorescence pattern, with both green and red areas visible. In contrast, biofilms treated with $_{0.1\ \%}$**K21** predominantly exhibit red fluorescence, signifying a high proportion of dead bacteria.

eosin. The parameters studied included the percentage of bone trabeculae, the number of inflammatory cells, collagen fiber bundles arrangement and amount of granulation tissue to evaluate healing and regeneration (Table 3).

At the 14th day, the bone formation had been initialized in every group. The defect in the experimental control group was filled with fibrinous connective tissue with very limited osseous fragments (8.66 %) (Fig. 9e). The entrance of wound area shows partial coverage of the defect with newly formed bone (Fig. 9h), which is forming in multiple loci in the wound area. Inflammation is severe showing a score of three (Fig. 9h). Large globular areas where multiple nidus of inflammatory cells are present having acute and chronic cells with a profound granulation tissue are seen (Fig. 9e). The collagen fibers are abundant, but their arrangement is disrupted (Table 4). The defects in the experimental **$_{0.1\ \%}$K21 scaffold group are filled with fibrinous connective tissue with newly formed bone which is not sufficient at this time but is significantly increased as compared to the control group (26.33 %) (Fig. 9f). The entrance of wound area shows almost complete coverage of defect with newly formed bone or osteoid. The new bone formation in the wound defect (Fig. 9i) is forming in multiple loci in the wound area. Inflammation is moderate showing a score of two (Fig. 9i), A nidus of inflammatory cells is also present having both acute and chronic cells located within a moderate granulation tissue (Fig. 9e).** The collagen fibers are abundant and well organized. The defect in the experimental **$_{0.1\ \%}$CHX** group is filled with fibrinous connective tissue with a very limited newly formed bone (16.67 %) (Fig. 9g). The entrance of wound area is not yet completely covered. The new bone formation in the wound defect is (Fig. 9j) forming in multiple loci in the wound area. Inflammation is moderate showing a score of two (Fig. 9b), and there is substantial granulation tissue. The collagen fibers are abundant and well organized (Table 4).

At the 21st day, there is active bone formation in every group. The opening of the defects in the experimental control group has been partially filled with new bone (41.48 %) and completely filled by bone like tissue (osteoid) (Fig. 9k). The new bone formation in the wound defects (Fig. 9n) is active in the central defect area, covered by freshly formed trabeculae. Mild inflammation is present with a score of one. The collagen fibers are less as almost half of the area has been filled with new trabeculae and there is organized arrangement of these fibers, with granulation tissue being scanty. The new bone formation in the experimental **$_{0.1\ \%}$K21** group has closed the openings of the wound areas completely. The newly formed bone has not yet filled the central area of the wound completely but there is significant increase as compared to the controls (59.67 %) (Fig. 9l). The trabeculae formation in the defect (Fig. 9o) is in multiple layers in an organized way determined by the orientation of collagen fibers. Inflammation is mild showing a score of one. The collagen fibers are abundant and well organized, and the granulation tissue is scanty (Table 5).

The opening defects in the experimental **$_{0.1\ \%}$CHX group has also been filled completely with the newly formed bone. However, the newly formed bone has not filled the central area of the wound completely (51.33 %) (Fig. 9p). The collagen fibers are moderate and well organized. Inflammation is mild showing a score of, and the granulation tissue is scanty (Table 4). On the 28th day, the majority of tissue has been completely filled with substantial trabecular bone, which is accompanied by adipose tissue. A thick bone covering is present at the surface area in all groups, the only difference is in experimental control group where the bone percentage is 91 % (Fig. 9q–t) as inflammatory cells and collagen fibers are absent; Fig. 9r, u $_{0.1\ \%}$K21 group; Fig. 9s, w $_{0.1\ \%}$CHX.**

3.10. Genomics

3.10.1. Gene expression distribution

Boxplots illustrate the distribution of gene expression levels (Table 6) and FPKM across many samples to compare gene expression levels under differing situations. For biological replicates, the final FPKM will represent the mean value (Figs. 10–11).

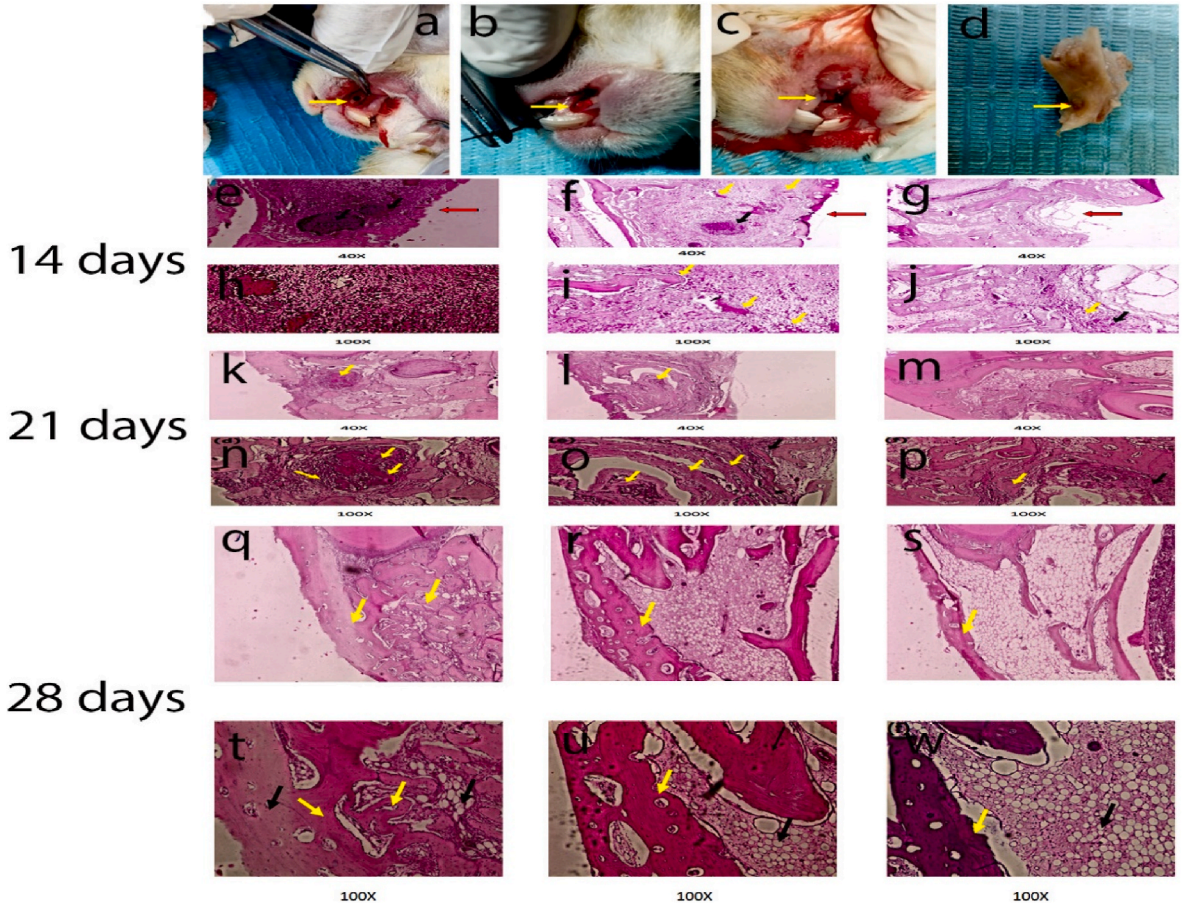

Fig. 9. (a–d) Macrophotographs (from left to right) of surgical wound created, and wound defect was filled with the therapeutic agent, wound area sutured, and maxilla was dissected showing the 3D bone mesh filled area. (e–j) Microphotographs of bone tissue at Day 14, haematoxylin and eosin (H&E)-stained: (e, h) control, (f, i) **$_{0.1\ \%}$CHX**, and (j, m) **$_{0.1\ \%}$K21**. Red arrow – surgical wound opening. Yellow arrow – bone trabeculae/Osteoid, and black arrow – inflammatory cells. (k–p) Microphotographs of bone tissue at Day 21, haematoxylin and eosin (H&E)-stained: (k, n) control, (l, o) **$_{0.1\ \%}$CHX**, and (m, p) **$_{0.1\ \%}$K21**. Yellow arrow – bone trabeculae/Osteoid, and black arrow – inflammatory cells. (q–w) Microphotographs of bone tissue at Day 28, haematoxylin and eosin (H&E)-stained: (q, t) control, (r, u) **$_{0.1\ \%}$CHX**, and (s, w) **$_{0.1\ \%}$K21**. Yellow arrow – bone trabeculae, and black arrow – Adipose tissue. At the 28th Day, most of the tissue has been filled with prosperous trabecular bone and accompanied by adipose tissues.

Table 3
Comparison of percentage of bone trabeculae (mean) amongst groups. At the 28th Day, most of the tissue has been filled with prosperous trabecular bone and accompanied by adipose tissues. A thick bony covering is present at the surface area in all groups, with the only difference being in experimental A group where the bone percentage is 91 % (Fig. 11a) (Table 4). Inflammatory cells and collagen fibers are absent.

Percentage of bone trabeculae	Control	$_{0.1\ \%}$K21	$_{0.1\ \%}$CHX	p-value
Day 14	8 ± 0.26	26.33 ± 0.25	16.67 ± 0.11	0.043*
Day 21	41 ± 0.12	59.67 ± 0.75	51.33 ± 0.15	0.092
Day 28	91 ± 0.1	100	100	0.001*

*p-value ≤0.05 is considered statistically *significant*.

Table 4
Pair wise comparison of percentage of bone trabeculae. Pair wise comparison has shown a significant difference between Group A and B at day 14 while there was no significant difference at day 21 and then again there was statistically significant difference between group A and B similarly in group A and C in percentage of the trabecular bone in surgically created wound, at the end of the experiment similarly.

	Groups	Groups	p-value
Day 14	Control	**$_{0.1\ \%}$K21**	0.036*
		$_{0.1\ \%}$CHX	0.324
	$_{0.}$K21	**$_{0.1\ \%}$CHX**	0.260
Day 21	Control	**$_{0.1\ \%}$K21**	0.08
		$_{0.1\ \%}$CHX	0.358
	$_{0.}$K21	**$_{0.1\ \%}$CHX**	0.493
Day 28	Control	**$_{0.1\ \%}$K21**	0.001*
		$_{0.1\ \%}$CHX	0.001*
	$_{0.}$K21	**$_{0.1\ \%}$CHX**	0.100

*p-value ≤0.05 is considered statistically *significant*.

3.10.2. Library construction, quality control and sequencing

Total RNA was extracted from control and K21-treated samples and subjected to integrity assessment using 1 % TAE agarose gel electrophoresis. As illustrated in Fig. 10A, strong and distinct bands corresponding to 28S (~4.7 kb) and 18S (~1.9 kb) ribosomal RNA were observed, with no signs of degradation, confirming high RNA quality across all samples. RNA purity and concentration metrics were evaluated using Nanodrop and Bioanalyzer systems and are detailed in Table 6. All samples showed OD260/280 ratios close to 2.1 and RNA integrity numbers (RIN) above 8.5, indicating minimal contamination and degradation, and ensuring suitability for downstream RNA sequencing.

Strand-specific mRNA libraries were prepared as shown in Fig. 10B. Poly-T oligo-conjugated magnetic beads were used to isolate polyadenylated transcripts, which were then fragmented enzymatically.

Table 5
Pearson Chi-Square test for association of inflammatory response. The association between inflammatory response and groups was analyzed by the Chi-Square test. According to the results of the tests, there was a significant association between inflammatory response and groups on day 14 and 21, while statistics were not computed on day 28 because of the constant values. The amount of granulation tissue and collagen fibers orientation had constant values on day 21 and 28 while a significant difference was found at day 14 between groups.

The number of inflammatory cells	Value	df	p-value
Day 14	9	2	0.011*
Day 21	9	2	0.018*

*p-value ≤0.05 is considered statistically significant.

First-strand cDNA synthesis was performed using random hexamer primers, followed by second-strand synthesis incorporating deoxyuridine triphosphates (dUTPs) to ensure strand specificity by blocking amplification of the second strand during PCR. After end-repair, A-tailing, adapter ligation, and size selection, the libraries were PCR-amplified and validated using Qubit fluorometry, real-time PCR, and a Bioanalyzer before sequencing on an Illumina platform.

3.10.3. Gene expression distribution

Gene expression levels were quantified using the normalisation method of FPKM (fragments per kilobase of transcript per million mapped reads). Fig. 10C shows boxplots of $\log_2(\text{FPKM} + 1)$ values for each sample, with controls (CTRL1–3) displayed in red and K21-treated samples (K21_1–3) in turquoise. The boxplots demonstrate consistent distributions and similar medians across all biological replicates, confirming high data quality and effective normalisation. Sample-to-sample correlations are presented in Fig. 10D, which shows a Pearson correlation heatmap (R^2 values). High intra-group correlation coefficients ($R^2 > 0.97$) and distinct inter-group differences confirm the reproducibility and biological divergence induced by K21 treatment.

3.10.4. Differential gene expression and statistical criteria

Differential gene expression analysis was conducted to identify genes altered in response to K21 treatment. Genes with a $\log_2$ fold change ($\log_2\text{FC}$) $\geq +1$ and adjusted p-value (padj) ≤ 0.05 were classified as significantly upregulated, while those with $\log_2\text{FC} \leq -1$ and padj ≤ 0.05 were considered downregulated. A total of 801 differentially expressed genes (DEGs) were identified, including 412 upregulated and 389 downregulated transcripts. These results are summarised in Fig. 10E, which presents a bar chart of DEG counts across regulation categories.

Fig. 11a visualises the overall distribution of DEGs as a volcano plot, with the x-axis representing $\log_2\text{FC}$ and the y-axis representing—$\log_{10}$(padj). Red and green dots denote significantly upregulated and downregulated genes, respectively, while grey dots represent genes without statistically significant change. The widespread distribution of DEGs along both axes reflects a substantial and biologically meaningful transcriptional response to K21.

Table 7 provides a curated list of DEGs relevant to osteogenesis and inflammation to highlight key regulators. Upregulated genes include *RUNX2*, *BMP2*, *COL1A1*, *SPP1*, and *ALPL*, all well-established osteogenic markers. In contrast, *IL6*, *TNF*, *CXCL8*, *MMP9*, and *NFKBIA* were significantly downregulated, suggesting a shift toward anti-inflammatory signalling. These transcriptional changes are consistent with the pro-regenerative and immunomodulatory properties observed in histological and functional assays.

3.10.5. Gene Ontology (GO) enrichment analysis

Gene Ontology (GO) enrichment analysis was performed to assess the functional significance of DEGs. Fig. 11B presents a bar plot of the top 30 enriched GO terms, categorised into biological processes (BP), cellular components (CC), and molecular functions (MF). Terms such as "ossification," "extracellular matrix organisation," and "bone development" were prominent within the BP category. Enriched CC terms included "collagen-containing extracellular matrix" and "basement membrane," while MF terms featured "calcium ion binding" and "extracellular matrix structural constituent."

Fig. 11E provides a bubble plot representation of GO enrichment results. The x-axis indicates the gene ratio (number of DEGs associated with each term divided by the total number of DEGs), bubble size corresponds to DEG count, and bubble colour denotes statistical significance (padj). Enriching osteogenesis- and matrix-related terms provides transcriptomic evidence supporting the histologically observed bone regeneration.

3.10.6. KEGG pathway enrichment analysis

Pathway enrichment analysis using the Kyoto Encyclopedia of Genes and Genomes (KEGG) database revealed major biological pathways modulated by K21 treatment. Fig. 11C displays a bar chart of the top enriched pathways, with significant representation of "ECM–receptor interaction," "TGF-beta signalling," and "HIF-1 signalling", all of which are essential for osteoblast differentiation, angiogenesis, and extracellular matrix remodelling. Also enriched were "cytokine–cytokine receptor interaction," "complement and coagulation cascades," and "neutrophil extracellular trap formation," pointing to a role for K21 in regulating immune responses and inflammation.

Fig. 11F presents the KEGG pathway data as a bubble plot. The x-axis represents gene ratio, bubble size denotes the number of DEGs involved, and bubble colour encodes statistical significance. These pathway enrichments align with the DEG profile shown in Table 7, reinforcing the conclusion that K21 simultaneously promotes bone regeneration and dampens inflammatory signalling through well-established molecular mechanisms.

Table 6
RNA Quantification Report; *rRNA Ratio for eukaryotes [28s/18s], plants [25s/18s], prokaryotes [23s/16s] Note: RNA is in nuclease-free water.

			Nanodrop (water as blank)			RNA Lab Chip Results						
No.	Sample Name	Organism	OD260/280	OD260/230	Conc. (ng/μL)	rRNA Ratio*	RIN	Initial Conc. (ng/μL)	Dilution Factor	Final Conc. (ng/μL)	Vol (μL)	Total Amount (μg)
1	C1	*Mus musculus*	2.149	2.283	1478.10	1.6	9.2	101.0	10	1010.00	45	45.45
2	C3	*Mus musculus*	2.151	2.255	1733.40	1.7	8.9	109.0	12	1259.60	45	56.68
3	C5	*Mus musculus*	2.212	1.976	911.92	1.9	9.3	127.0	9	1158.14	45	52.12
4	3T3 1	*Mus musculus*	2.183	1.613	668.48	1.6	8.6	112.0	7	748.70	45	33.69
5	3T3 3	*Mus musculus*	2.166	2.266	620.80	1.6	8.9	112.0	6	695.30	45	31.29
6	3T3 5	*Mus musculus*	2.184	2.144	719.48	1.7	8.6	119.0	7	856.18	45	38.53

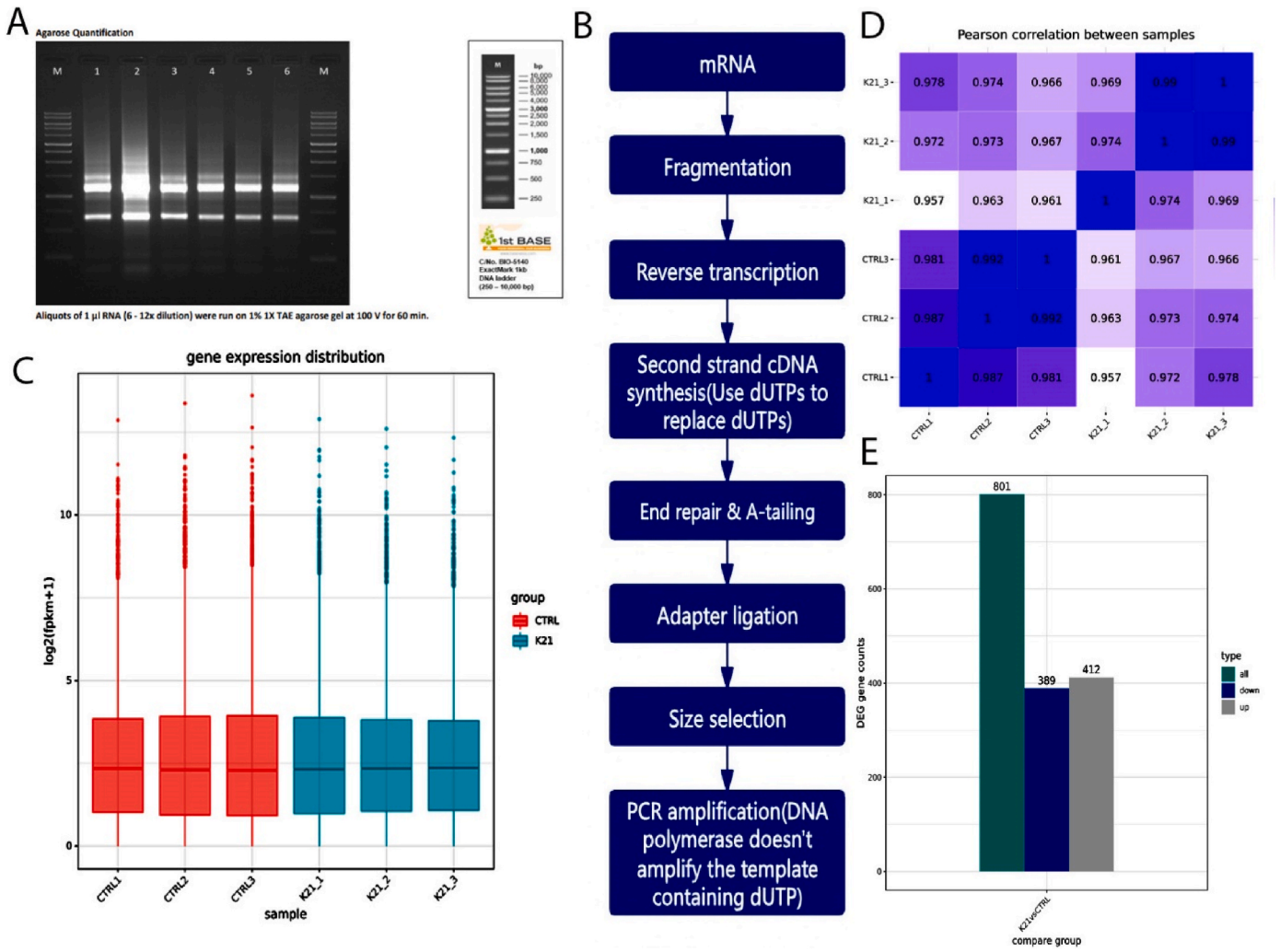

Fig. 10. (A) Library construction, quality assurance, and sequencing. Messenger RNA was isolated from total RNA utilising poly-T oligo-conjugated magnetic beads. Following fragmentation, the initial strand of cDNA was synthesised utilising random hexamer primers, succeeded by the synthesis of the second strand of cDNA employing dTTP for a non-strand specific library. The non-strand specific library was prepared following end repair, A-tailing, adapter ligation, size selection, amplification, and purification. The library was analyzed using Qubit and real-time PCR for quantification, and a bioanalyzer for size distribution assessment. Quantified libraries will be aggregated and sequenced on Illumina platforms, based on optimal library concentration and data volume. (B) Workflow for non-directional library building. (C) Box plot illustrating the dispersion of gene expression samples. The X axis denotes the sample name, while the Y axis signifies log2 (FPKM+1). The parameters of the box plots are specified, including maximum, upper quartile, median, lower quartile, and minimum. (D) Inter-sample correlation heat map R^2: Square of the Pearson correlation coefficient (R). Histogram of Differential Gene Number Statistics for Difference Comparison. Blue and grey denote the up-regulated and down-regulated differential genes, respectively, while the column numbers reflect the quantity of differential genes.

4. Discussion

In most tissue engineering applications, scaffolds are designed to provide structural support and also to mimic natural extracellular matrix, the latter making them suitable for delivering drugs or growth factors while they serve as structural scaffolds that are eventually replaced with new tissue [23]. Scaffolds for osteogenesis should mimic the morphology, structure, and function of bone to optimize tissue integration. However, the architecture of bone is highly complex, with cortical bone being compact and 3–12 % porous, featuring voids like the 100–200 µm Haversian canals; while trabecular bone exhibits 50–90 % porosity with pores around 1 mm. Variations in porosity, mechanical properties, mineral density, and biological factors and patient-specific differences (age, nutrition, health) pose challenges in fabricating scaffolds for specific repair needs. Hence, the critical goal in addressing the complexity of bone tissue is to ensure the rapid replacement of the bone substitute with newly formed mature bone [24]. While the scaffold's composition will dictate its biocompatibility, the porosity, or the percentage of void space in a solid, play a key role if they can allow proper cell penetration, migration, nutrient diffusion, proliferation, vascularization as well as bone ingrowth. From a macroscopic perspective, factors such as overall architecture, pore morphology, interconnectivity, and pore size distribution play distinct roles in facilitating bone ingrowth. The adsorption and retention of proteins within the material's microporosities will determine subsequent cell adhesion from a microscopic standpoint [25].

In one study, elevated porosity did not influence cell attachment but led to increased cell proliferation, as the pore space enhanced the transport of oxygen and nutrients; conversely, lower porosity exhibited heightened alkaline phosphatase activity and greater osteocalcin expression, resulting in diminished proliferation and augmented osteogenesis [26]. Unlike traditional methods for creating porosity, our 3D-printed scaffold offers enhanced design control, resulting in markedly improved mechanical qualities. Total porosity, pore dimensions, pore size distribution, and pore morphology are essential in harmonising the physical and biological characteristics of scaffolds to facilitate

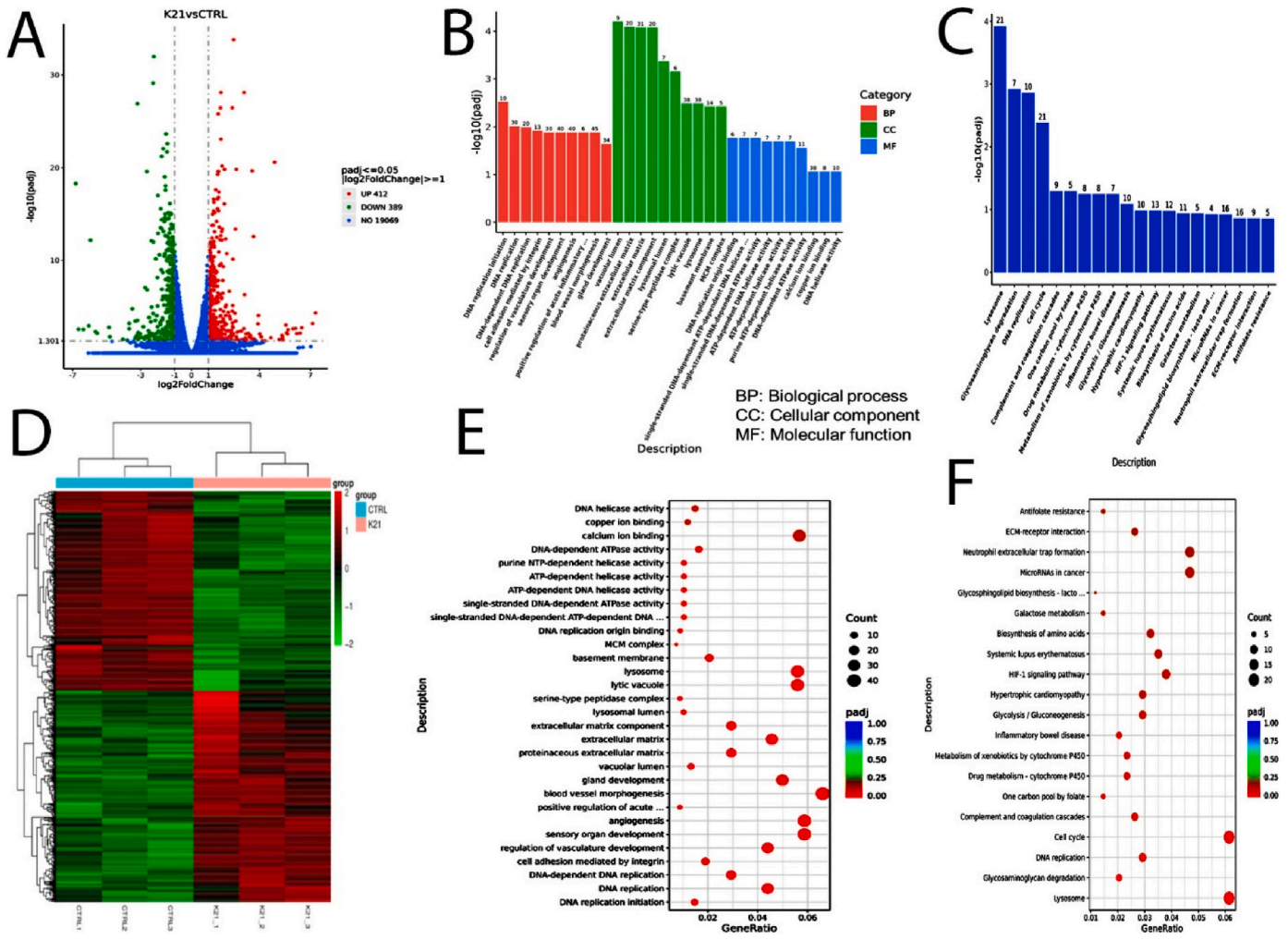

Fig. 11. (A) Differential Gene Volcano Map. The abscissa in the figure represents log2FoldChange, while the ordinate denotes -log10padj or -log10pvalue; the blue dashed line signifies the threshold for differential gene screening criteria. (B) Histogram of Gene Ontology (GO) enrichment analysis. The abscissa in the image represents the GO Term, while the ordinate indicates the amount of importance of enrichment for the GO Term, denoted as -log10(padj). (C) Various colours signify distinct functional categories. Histogram of KEGG enrichment analysis. The abscissa represents the KEGG pathway, whereas the ordinate denotes the significant level of pathway enrichment. (D) Differentially expressed gene clustering heatmap. The comprehensive outcomes of the FPKM cluster analysis were derived using the log2 (FPKM+1) value. The red colour signifies samples with elevated expression levels, whereas the green colour denotes low expression levels. The colour gradient from red to green signifies that log2 (FPKM+1) values range from high to low. Enrichment Analysis Scatter Plot for Gene Ontology (E). The abscissa of the graph represents the ratio of the differential gene count to the overall number of differential genes associated with the GO Term, while the ordinate denotes the GO Term itself. KEGG enrichment scatter plot (F). The abscissa on the graph represents the ratio of differential genes within the KEGG pathway to the overall number of differential genes, while the ordinate denotes the KEGG pathway.

Table 7
Key differentially expressed genes.

Gene Symbol	Gene Name	Log2 Fold Change	Adjusted p-value (padj)	Regulation	Biological Function
COL1A1	Collagen type 1 alpha 1 chain	3.2	0.0005	upregulated	Collagen synthesis
RUNX2	Runt-related transcription factor 2	2.8	0.0008	unregulated	Osteoblast differentiation
SPP1	Secreted phosphoprotein 1	2.5	0.001	upregulated	Bone matrix protein (Osteopontin)
BMP2	Bone morphogenic protein 2	2.3	0.0012	upregulated	Osteogenic growth factor
ALPL	Alkaline phosphatase, liver/bone/kidney	2.0	0.0015	upregulated	Bone mineralization enzyme
IL6	Interleukin 6	−2.1	0.002	downregulated	Prof-inflammatory cytokine
TNF-α	Tumour necrosis factor alfa	−2.4	0.0018	downregulated	Inflammation mediator
MMP9	Matrix metallopeptidase 9	−2.6	0.0016	downregulated	ECM degradation enzyme
CXCL8	C-X-C motif chemokine ligand 8 (IL-8)	−2.8	0.0011	downregulated	Neutrophil chemotaxis
NFKBIA	NF-kappa-B inhibitor alpha	−3.0	0.0009	downregulated	NF- κB pathway inhibitor

effective tissue regeneration. The $_{0.1\ \%}$**K21** group had the greatest porosity and a most uniform surface shape. Scaffolds with a high uniformity of pore size facilitate rapid colonisation, given that the pores are adequately large; conversely, a heterogeneous pore size distribution can enable cell colonisation, although an increased proportion of smaller pores may impede the diffusion of nutrients, oxygen, and cellular waste. Efficient regulation of fluid flow through the scaffold, governed by pore interconnectivity and permeability, is crucial for enabling adequate cell

infiltration. Moreover, optimising pore morphology can further improve cell infiltration, facilitating uniform colonisation throughout the scaffold [22].

The Raman spectra results provide an insight into the structural quality of the scaffolds in presence of K21 and chlorhexidine by examination of the intensities of $v_1PO_4^{3-}$ (960 cm^{-1}) and $v_1CO_3^{2-}$ (1045 cm^{-1}) peaks along with their calculated ratios. The vibrational band at 960 cm^{-1} represents the symmetric stretching of phosphate ions lattice, serving as a key marker of its structural stability. In this study, the control and **$_{0.1\ \%}$CHX** groups demonstrated comparable $v_1PO_4^{3-}$ intensities (498 ± 6.5 and 501 ± 11.1, respectively), suggesting a stable and well-formed phosphate phase. However, the significantly lower intensity observed in the **$_{0.1\ \%}$K21** group (463 ± 3.9) suggests subtle modifications in the hydroxyapatite structure. Conversely, the carbonate peak at 1045 cm^{-1} ($v_1CO_3^{2-}$) was significantly higher in the **$_{0.1\ \%}$K21** group (61.3 ± 5.9 b) compared to the control (33.1 ± 2.5 a) and CHX groups (55.4 ± 8.1 a). This increase leads to a higher $v_1CO_3^{2-}/v_1PO_4^{3-}$ ratio (62.5 ± 6.1 θ), indicating a positive effect of K21 on the hydroxyapatite scaffold. Carbonate substitution into the hydroxyapatite lattice has been associated with improved bioactivity and resorption potential, key factors for bone regeneration [27,28]. In addition, the stable phosphate vibration at 960 cm^{-1} and the enhanced ratio observed in the **$_{0.1\ \%}$K21** group suggests that the calcium phosphate scaffold remains structurally stable while potentially enhancing its regenerative capacity. The calcium-based scaffolds are widely understood for their ability to serve as osteoconductive materials, providing a suitable template for bone cell adhesion, proliferation and mineral deposition [29]. In animal models, similar modifications in hydroxyapatite structure have demonstrated increased bone regeneration potential, particularly when the scaffold supports carbonate incorporation and maintains structural stability [30]. The Raman and XRD findings for the **$_{0.1\ \%}$K21** group align with these observations, as the scaffold appears to accept carbonate incorporation without compromising the phosphate structure, thereby maintaining the lattice stability of hydroxyapatite which is important for its success as a biomaterial in bone tissue engineering. Additionally, the increased $v_1CO_3^{2-}/v_1PO_4^{3-}$ ratio further suggests levels of maturity and bioactivity, which could enhance the integration of the scaffold within the bone microenvironment, so accelerating healing and regeneration processes [31,32]. The XRD data show a changed, more aligned extracellular matrix that supports mineralization in the presence of K21, antimicrobials, and β-tricalcium phosphate. The diffraction peaks of calcium, suggest it may enhance the mineralization potential of the scaffold, presenting a duality; on one hand, the presence of calcium phosphates can facilitate bone and dental tissue regeneration. These scaffolds will be highly pertinent following the integration of antimicrobial compounds, such as K21 platform chemistry, to offer protection against infections post-surgical implantation.

K21 exhibits a potent antibacterial effect as demonstrated by its ability to significantly reduce bacterial viability and disrupt biofilm structure [33]. The molecule interacts with the biofilm matrix, breaking down its cohesive structure and leading to the death of embedded bacterial cells [34]. In fluorescence microscopy, K21-treated biofilms predominantly display red fluorescence, indicating a high proportion of dead bacteria. This suggests that K21 not only inhibits bacterial growth but also effectively penetrates and dismantles biofilms, which are notoriously resistant to conventional antimicrobial agents like CHX. Such activity makes K21 a promising candidate for combating biofilm-associated infections, particularly in periodontal disease. The reduction of biofilm is critical for bone regeneration, especially in conditions like periodontitis, where biofilm-associated bacteria trigger host immune system, leading to chronic inflammation and excessive osteoclastic activity, resulting in bone resorption and bone loss [35]. By eradicating the biofilm, K21 reduces the bacterial load, minimize inflammation, preventing the release of virulence factors (e.g., proteases and toxins) that degrade bone tissue and inhibit osteogenesis. In the absence of biofilms, osteoblasts can proliferate and deposit new bone matrix. Additionally, reduced inflammation supports the differentiation and activity of osteoblasts. The removal of biofilm will enhance the availability of growth factors, nutrients, and oxygen, essential for tissue repair and regeneration [36]. In addition, when cytolysins are added to the biofilm assays, increased antibacterial activity is observed. That may promote the formation of quorum within the microenvironment of the bacterial cell aggregates. However, the virulence was substantially reduced ($p < 0.05$) when exposed to **$_{0.1\ \%}$K21** scaffold, particularly at concentrations like that of **$_{0.1\ \%}$CHX**. Ongoing efforts are necessary to delineate how the cytolysin compromises target cells and to identify the specific mechanism or mechanisms by which the cytolysin induces toxicity across diverse infection systems. Further studies are needed to evaluate the long-term effects and potential cytotoxicity of K21.

From the in vivo experimental results of percentages of bone trabeculae, the control groups showed limited bone formation (8.66 %). The inflammation score was three and the collagen fibers were disrupted which suggests slower regeneration and a lower initial healing response. **$_{0.1\ \%}$K21** and **$_{0.1\ \%}$CHX** scaffolds had improved bone formation (26.33 % and 16.67 % respectively) compared to the control groups. Both groups displayed well-organized collagen and moderate inflammation with a score of two. The percentage of bone trabeculae in both groups on day 28 were superior to group A (Table 4). The findings demonstrated that the scaffolds with 0.1 % chlorhexidine and in particular **$_{0.1\ \%}$K21** had little inflammation and a higher percentage of bone trabecular within a well-structured tissue. The proinflammatory cytokines may have been essential in mediating the creation of inflammatory cells, thereby facilitating wound healing and offering protection at both local and systemic levels. The figure indicates that on day 14, the 0.1 % chlorhexidine and **$_{0.1\ \%}$K21** groups exhibited reduced inflammation levels relative to the control group. The anti-inflammatory features may be due to acceleration in wound healing under their influence of a reduction in the inflammatory response [17]. The control group displayed substantial granulation tissue but with disrupted collagen fibers indicating inefficient remodelling. The efficient incorporation of silane into the collagen matrix generates new bonding arrangements, namely C–Si–O, Si–O–Si, and Si–O–C bonds, which trigger the polycondensation of silanol groups and the cross-linking of –OH groups in collagen fibres. The proinflammatory cytokines likely played a crucial role in facilitating the formation of inflammatory cells, thereby aiding in wound healing and offering protection at both local and systemic levels. The figure indicates that on day 14, the 0.1 % chlorhexidine and **$_{0.1\ \%}$K21** groups exhibited reduced inflammation levels relative to the control group [37]. Like any animal model however, the one used here has certain limitations that may impede the accurate investigation of immune responses and inflammatory mechanisms. Certain biological analysis methods, such as those detecting antibodies, are deficient. Specific genes implicated in critical inflammatory pathways require more evaluation, indicating that certain molecular tasks may be performed by distantly related or entirely unrelated effectors. The advancement of single-cell-omics methodologies has, however, enabled the mitigation of certain shortcomings, facilitating our model for investigating inflammation in relation to normal physiopathology [38,39].

The utilisation of organofunctional silanes, characterised by extended hydrocarbon chains, in K21 scaffolds would improve surface hydrophobicity by modifying the surface energy of the scaffolds. Increased surface energy would thus enhance the wettability of the demineralised dentin surface and promote superior attachment [40]. Organofunctional silanes work as water scavengers, reacting with water molecules to hydrolyse the alkoxy groups attached to the silanes, thus converting them into alcohol molecules [41]. The integration of hydrophobic quaternary ammonium salts within the scaffold led to the development of a more hydrophobic substrate leading to superior encapsulation of collagen fibrils, augmented mechanical characteristics of the scaffold, and enhanced mechanical endurance. The scaffold mechanical properties is typically designed to match the elastic modulus of human cancellous bone (0.1–2 GPa) or cortical bone (15–20 GPa). This

alignment will ensure mechanical compatibility with the host tissue, enabling proper load transfer and reducing the risk of mechanically induced complications, such as stress shielding or implant-related osteopenia.

The actin-based microfilament system is a crucial component of the cytoskeleton in human gingival fibroblasts, playing a pivotal role in cell adhesion and mobility. During the inflammation and proliferation stages of wound healing, effectively managing the inflammatory response is essential to protect fibroblasts from inflammatory agents [35]. This protection facilitates the transition from the proliferation phase to the remodelling stage, leading to increased collagen fiber deposition and improved tissue repair, which were as observed in **$_{0.1\ \%}$K21** scaffolds. This suggests that the regenerated tissue demonstrated enhanced efficacy through its capacity to eradicate pathogens, facilitate collagen fibre deposition, and diminish inflammation [35]. The fibroblastic cell structure showed biocompatibility to the K21 molecules as seen being ingested in the first hour. The molecule showed effective breakdown and clearance which confirmed the positive activity of the cells.

The levels of all differently expressed genes in the comparison group were aggregated to form the differential gene set. Hierarchical clustering was employed to group the FPKM values of samples and standardise the rows using Z-scores. The samples exhibiting analogous expression patterns in the heat map were aggregated. The hue in each grid represented not the gene expression value, but the value derived from normalising the expression data rows (often ranging from −2 to 2). Consequently, the colours in the heat map can only be compared horizontally (the expression of the same gene across various samples), but not vertically (the same sample). There exist both inter-group clustering and inter-sample clustering. The final report illustrates the clustering of samples. The findings underscore the importance of balancing inflammation, promoting collagen organization, and reducing granulation tissue for optimal bone regeneration. The **$_{0.1\ \%}$K21** scaffolds consistent superiority in those respects highlights the potential of targeted interventions to enhance healing outcomes.

Bone reconstruction requires materials with properties closely aligned to the native bone's structure and physical characteristics, such as elastic modulus and internal porosity. However, most currently available bone substitutes exhibit challenges, including limited or unpredictable resorption times, shaping difficulties, and inadequate internal porosity. These limitations are further hampered by suboptimal effectiveness in bone tissue regeneration in clinical cases involving insufficient supporting bone around defects, and possible presences of osteo metabolic diseases, or diabetes. Synthetic scaffolds have the potential to address many of these limitations by creating a microenvironment mimicking native bone, while avoiding triggering significant inflammatory response yet providing structural rigidity to withstand external stresses like native bone tissue. In this regard, 3D-printing technologies [42] with K21 additions represent a significant advancement compared with conventional regenerative surgical techniques for bone-related treatments.

5. Conclusion

Within the limits of the study, 3D-printing technologies with **$_{0.1\ \%}$K21** represent a significant advancement over conventional regenerative medicine techniques for bone-related treatments.

Data and materials availability

Any researcher can replicate or augment the analysis employing the data, code, and resources utilised in the study. The datasets produced and/or analyzed in this study are not publicly accessible due to confidentiality but can be obtained from the corresponding author upon a reasonable request.

Declaration of competing interest

The authors whose names are listed in the manuscript have no affiliation or involvement in an organization or entity with a financial or non-financial interest in the subject matter or materials discussed in this manuscript.

Acknowledgements

The authors extend their gratitude to the laboratories at IMU University, Malaysia and MIMOS Laboratory for their support in executing study experiments and analyses. The study was funded by IMU University (4.12/JCM-285/2024) and Network for Canadian Oral Health Research: New Frontier Seed Grant Program 2023-24 and Dalhousie University Start-up Funding (Zeeshan Sheikh). We would like to thank Professor Frederick Smales for his valuable assistance in reviewing this manuscript for English language clarity and accuracy.

Appendix A. Supplementary data

Supplementary data to this article can be found online at https://doi.org/10.1016/j.reth.2025.08.001.

References

[1] Torabi K, Farjood E, Hamedani S. Rapid prototyping technologies and their applications in prosthodontics, a review of literature. J Dent (Shiraz, Iran) 2015;16(1):1–9.
[2] Pillai S, Upadhyay A, Khayambashi P, et al. Dental 3D-Printing: transferring art from the laboratories to the clinics. Polymers 2021;13(1):157.
[3] Denry I, Kuhn LT. Design and characterization of calcium phosphate ceramic scaffolds for bone tissue engineering. Dent Mater 2016;32(1):43–53.
[4] Alok K, Sourav M, Srimanta B, et al. Low temperature additive manufacturing of three-dimensional scaffolds for bone-tissue engineering applications: processing related challenges and property assessment. Mater Sci Eng 2016;103:1–39.
[5] Martínez-Vázquez FJ, Cabañas MV, Paris JL, et al. Fabrication of novel Si-doped hydroxyapatite/gelatine scaffolds by rapid prototyping for drug delivery and bone regeneration. Acta Biomater 2015;15(3):200–9.
[6] Rahimnejad M, Makkar H, Dal-Fabbro R, et al. Biofabrication strategies for oral soft tissue regeneration. Adv Healthc Mater 2024;13(18):e2304537.
[7] Vandana K, Chandra GNRB. Periodontal osseous defects: a review. J Dent 2017;1:9.
[8] Schallhorn RA, McClain PK. Periodontal regeneration: management of periodontal osseous defects by the periodontist-dental hygienist team. J Evi Based Dent Prac 2023;14(1):42–52.
[9] Beck J, Garcia R, Heiss G, et al. Periodontal disease and cardiovascular disease. J Periodontol 1996;67(3):1123–7.
[10] França R, Samani TD, Bayade G, et al. Nanoscale surface characterization of biphasic calcium phosphate, with comparisons to calcium hydroxyapatite and β-tricalcium phosphate bioceramics. J Colloid Inter Sci 2014;420:182–8.
[11] Spaeth K, Goetz-Neunhoeffer F, Hurle K. The effect of Cu2+ doping in β-tricalcium phosphate on the hydration mechanism of a brushite cement. Mater Today 2023;27(1):101288.
[12] Sblendorio GA, Santoni B, Le G, et al. Towards animproved understanding of the β-TCP crystal structure by means of "checkerboard" atomistic simulations. J Eur Ceramic Soci 2023;8(4):3746.
[13] Yashima M, Sakai A, Kamiyama T, et al. Crystal structure analysis of βtricalcium phosphate Ca3(PO4)2 by neutron powder diffraction. J Solid State Chem 2003;175(2):272–7.
[14] Bae J, Ida Y, Sekine K, et al. Effects of high-energy ball-milling on injectability and strength of β-tricalcium phosphate cement. J Mec Behav Bio Mater 2015;47(4):77–86.
[15] Bapat RA, Parolia A, Chaubal T. Recent update on applications of Quaternary ammonium silane as an antibacterial biomaterial: a novel drug delivery approach in dentistry, vol. 13. Front. Micro; 2002.
[16] Bapat RA, Mak KK, Pichika MR, et al. Newly discovered clouting interplay between matrix metalloproteinases structures and novel Quaternary Ammonium K21: computational and in-vivo testing. BMC Oral Health 2024;24(1):382.
[17] Daood U, Yiu C, Burrow MF, et al. Effect of a novel quaternary ammonium silane cavity disinfectant on durability of resin–dentine bond. J Dent 2017;60:77–86.
[18] Daood U, Ilyas MS, Ashraf M, et al. Biochemical changes and macrophage polarization of a silane-based endodontic irrigant in an animal model. Sci Rep 2024;12:6354.
[19] Dai Y, Wang P, Mishra A, et al. 3D bioprinting and artificial intelligence-assisted biofabrication of personalized oral soft tissue constructs. Adv Healthc Mater 2024;17:2402727.
[20] Sarita S, Simon Y, Julia G, et al. A composite critical-size rabbit mandibular defect for evaluation of craniofacial tissue regeneration. Nat Protoc 2016;11(10):1989–2009.

[21] Muhammad S, Ayesha F, Uzma A, et al. Effect of honey on healing of extracted tooth socket of albino wistar rats. Inter Med J 2017;22(5):422–5.
[22] Jakub T, Petr C, Jaroslav P, et al. The effect of hyperbaric oxygen therapy on acute wound healing in rabbits: an experimental study and histopathological analysis. Mil Med Sci Lett 2021;1:2.
[23] Ulery BD, Nair LS, Laurencin CT. Biomedical applications of biodegradable polymers. Journal of Polymer Science Part B: Pol Phy 2011;49(12):832–64.
[24] Kasten P, Beyen I, Niemeyer P, et al. Porosity and pore size of β-tricalcium phosphate scaffold can influence protein production and osteogenic differentiation of human mesenchymal stem cells: an in vitro and in vivo study. Acta Biomater 2008;4(6):1904–15.
[25] Perez RA, Mestres G. Role of pore size and morphology in Musculo-skeletal tissue regeneration. Mater Sci Eng C 2016;61:922–39.
[26] Karageorgiou V, Kaplan D. Porosity of 3D biomaterial scaffolds and osteogenesis. Biomater 2005;26(27):5474–91.
[27] Dorozhkin S. Calcium orthophosphate-based bio ceramics. Materials 2013;6(9): 3840–942.
[28] Bohner M, Santoni BLG, Döbelin N. β-tricalcium phosphate for bone substitution: synthesis and properties. Acta Biomater 2020;113:23–41.
[29] Habraken W, Habibovic P, Epple M, et al. Calcium phosphates in biomedical applications: materials for the future? Mater Today 2016;19(2):69–87.
[30] Huang Y, Jin X, Zhang X. Osteogenic differentiation of bone marrow stromal cells on hydroxyapatite scaffolds with carbonate incorporation. J Biomed Mater Res 2020;18(6):757–67.
[31] Zhao R, Yang R, Cooper PR. Carbonate substitution in hydroxyapatite scaffolds: mechanisms and regenerative potential. Adv Healthc Mater 2020;23(15):2101487.
[32] Kasten P. Comparison of human bone marrow stromal cells seeded on calcium-deficient hydroxyapatite, β-tricalcium phosphate and demineralized bone matrix. Biomater 2003;24(15):2593–603.
[33] Daood U, Matinlinna JP, Pichika MR, et al. A Quaternary ammonium silane antimicrobial triggers bacterial membrane and biofilm destruction. Sci Rep 2020; 10:10970.
[34] Daood U, Parolia A, Matinlinna J, et al. Antibacterial and antibiofilm efficacy of k21-E in root canal disinfection. Dent Mater 2020;37(10):e386.
[35] Yutao C, He L, Yuhang T, et al. Dual-functional composite scaffolds for inhibiting infection and promoting bone regeneration. Mater Today Bio 2022;16:100409.
[36] Matzelle MM, Gallant MA, Condon KW, et al. Resolution of inflammation induces osteoblast function and regulates the wnt signalling pathway. Arthritis Rheum 2012;64(5):1540–50.
[37] Dhand C, Balakrishnan Y, Theng Ong S. Antimicrobial quaternary ammonium organo silane cross-linked nanofibrous collagen scaffolds for tissue engineering. Int J Nanomedicine 2018;13:4473–92.
[38] Buchan KD, van Gent M, Prajsnar TK. Human specific staphylococcal virulence factors enhance pathogenicity in a humanised zebrafish C5a receptor model. J Cell Sci 2021;134(5):453.
[39] Choi TY, Choi TI, Lee YR, et al. Zebra fish as an animal model for biomedical research. Exp Mol Med 2021;53:310.
[40] Lung CYK, Matinlinna JP. Silanes for adhesion promotion and surface modification. Silane, chemistry, applications and performance. In: Moriguchi K, Utagawa SS, editors. Silane, chemistry, applications and performance. New York: Nova Science Publishers; 2013. p. 87–110.
[41] Mancheno-Posso P, Dittler RF, Lewis D, et al. Review of status, trends, and challenges in working with silane and functional silanes. In: Moriguchi K, Utagawa SS, editors. Silane, chemistry, applications and performance. New York: Nova Science Publishers; 2013. p. 66.
[42] Xu HH, Wang P, Wang L, et al. Calcium phosphate cements for bone engineering and their biological properties. Bone Res 2017;5.